



HAL
open science

Temperatures and cooling rates recorded by the New Caledonia ophiolite: implications for cooling mechanisms in young forearc sequences.

Arianna Secchiari, Alessandra Montanini, Dominique Cluzel

► To cite this version:

Arianna Secchiari, Alessandra Montanini, Dominique Cluzel. Temperatures and cooling rates recorded by the New Caledonia ophiolite: implications for cooling mechanisms in young forearc sequences.. Geochemistry, Geophysics, Geosystems, In press, 10.1029/2021GC009859 . hal-03524046

HAL Id: hal-03524046

<https://unc.hal.science/hal-03524046>

Submitted on 13 Jan 2022

HAL is a multi-disciplinary open access archive for the deposit and dissemination of scientific research documents, whether they are published or not. The documents may come from teaching and research institutions in France or abroad, or from public or private research centers.

L'archive ouverte pluridisciplinaire **HAL**, est destinée au dépôt et à la diffusion de documents scientifiques de niveau recherche, publiés ou non, émanant des établissements d'enseignement et de recherche français ou étrangers, des laboratoires publics ou privés.

1
2
3
4
5
6
7
8
9
10
11
12
13
14
15
16
17
18
19
20
21
22
23

Temperatures and cooling rates recorded by the New Caledonia ophiolite: implications for cooling mechanisms in young forearc sequences.

Arianna Secchiari ^a, Alessandra Montanini ^a, Dominique Cluzel ^b

^a Department of Chemistry, Life Sciences and Environmental Sustainability, University of Parma, Italy

^b Institut des Sciences Exactes et Appliquées, Université de la Nouvelle-Calédonie, New Caledonia

Corresponding author: Alessandra Montanini (alessandra.montanini@unipr.it)

Key Points:

- A comprehensive geothermometric investigation of the New Caledonia ophiolite has been carried out.
- The computed temperatures and cooling rates ($\approx 10^{-4}$ - 10^{-3} °C/y) contrast with previous results on ophiolitic and forearc peridotites.
- The thermal conditions recorded by forearc sequences can be linked to specific areal processes and previous lithosphere evolution.

24 **Abstract**

25 To unveil how forearc lithosphere cools and re-equilibrates, we carried out a comprehensive geothermometric
 26 investigation of the New Caledonia ophiolite, which represents a rare example of proto-arc section generated
 27 during subduction infancy. A large dataset, including more than eighty samples (peridotites and mafic-
 28 ultramafic intrusives), was considered.

29 Closure temperatures calculated for the lherzolites using slow ($T_{\text{REE-Y}}$) and fast diffusing ($T_{\text{Ca-in-Opx}}$, T_{BKN} , $T_{\text{Ca-}}$
 30 in-Ol , $T_{\text{Ol-Sp}}$) geothermometers provide some of the highest values ever documented for ophiolitic peridotites,
 31 akin to modern sub-oceanic mantle. Cooling rates deduced from $T_{\text{REE-Y}}$ and T_{BKN} yield values of $\approx 10^{-3}$ °C/y,
 32 similar to those obtained with $T_{\text{Ca-in-Ol}}$. These features are consistent with a post-melting history of
 33 emplacement, possibly along a transform fault, and thermal re-equilibration via conduction.

34 Cpx-free harzburgites register a high-T evolution, followed by quenching and obduction. The relatively high
 35 $T_{\text{Ca-in-Ol}}$, $T_{\text{Ol-Sp}}$ and cooling rates computed from $T_{\text{Ca-in-Ol}}$ ($\approx 10^{-3}$ °C/y) are atypical for this geodynamic setting,
 36 mirroring the development of an ephemeral subduction system, uplift and emplacement of the Peridotite
 37 Nappe.

38 Temperature profiles across the crust-mantle transect point to high closure temperatures, with limited
 39 variations with depth. These results are indicative of injection and crystallization of non-cogenetic magma
 40 batches in the forearc lithosphere, followed by thermal re-equilibration at rates of $\approx 10^{-4}$ - 10^{-3} °C/y.

41 Our study shows that the thermal conditions recorded by forearc sequences are intimately related to specific
 42 areal processes and previous lithospheric evolution. Thus, detailed sampling and exhaustive knowledge of the
 43 geological background are critical to unravel the cooling mechanisms in this geodynamic setting.

44

45 **Plain Language Summary**

46

47 The New Caledonia ophiolite represents a rare example of complete forearc section, extending from the lower
 48 crust to the mantle, originated at the beginning of the Eocene subduction. Our study aims to shed light on the
 49 thermal evolution of this ophiolite, which constitutes one of the largest ophiolite complexes worldwide, gaining
 50 – at the same time - insights into the mechanisms that govern cooling of forearc lithosphere. For this purpose,
 51 different geothermometers were applied to mantle peridotite and mafic-ultramafic intrusive samples.
 52 Geothermometers are equations based on temperature-dependent major element and/or trace element exchange
 53 reactions among mineral phases, which allow calculating equilibrium temperatures starting from mineral
 54 chemical compositions. Equilibrium temperatures obtained with various thermometers can be linked to the
 55 cooling evolution and heat extraction rates of the studied samples. With this study, we were able to track the
 56 post-melting evolution and re-equilibration at lower temperature conditions for all the investigated rock types.
 57 A comprehensive investigation of the Massif du Sud sequence, from the lower crust to the upper mantle,
 58 allowed us to build thermal profiles across the forearc lithosphere. Overall, our results contribute to unravel
 59 the cooling mechanisms of the crust-mantle sequences in this poorly explored tectonic setting.

60

61 1 Introduction

62 Chemical geothermometers are powerful tools to unravel the thermal history of mafic and ultramafic
63 lithologies. They allow to calculate closure temperatures starting from measured mineral compositions using
64 temperature-dependent major elements (e.g. Wells, 1977; Brey & Köhler, 1990; Putirka, 2008) and/or trace
65 element exchange reactions among mineral phases (e.g. Lee et al., 2007; Liang et al., 2013; Sun and Liang,
66 2014).

67 Results obtained from major and trace element thermometry strongly depend on the thermal evolution and
68 cooling rates experienced by the analyzed samples. Chemical geothermometers applied to rock samples
69 thermally equilibrated over long geological times, which undergo rapid exhumation and/or eruption, are
70 expected to yield homogeneous temperatures, corresponding to their equilibration conditions. Hence, no
71 information related to their thermal evolution will be available for such samples. This is the case of mantle
72 xenoliths from continental lithosphere brought to the surface by intraplate volcanism (e.g. Liang et al., 2013
73 and references therein; Guo et al., 2019).

74 By contrast, for samples that cooled relatively slowly to allow appreciable diffusive re-equilibration to occur
75 among mineral phases during cooling, the application of different chemical thermometers will provide a range
76 of temperatures. More specifically, geothermometers will show higher temperatures for samples with faster
77 cooling rates. In this case, geothermometers will be able to track the thermal evolution of the studied
78 lithologies.

79 Temperatures calculated with a given thermometer are related to the intercrystalline diffusion rates of the
80 elements (or components) used to calibrate the thermometer. In detail, slowly diffusing element-based
81 thermometers can preserve the highest closure temperatures (e.g. the REE+Y Cpx-Opx thermometer: Liang et
82 al., 2013), while fast diffusing element-based thermometers will indicate low equilibration temperatures
83 (Dygert and Liang, 2015; Hanghøj et al., 2010; Liang et al., 2013).

84 Although the combined application of different thermometers represents a powerful tool to shed light on the
85 thermal regimes experienced by the ophiolitic complexes during their lifetime, only a few studies have been
86 performed. These works mostly focused on ophiolites with little or no subduction influence, or formed at fossil
87 Mid Ocean Ridges (e.g. Dygert and Liang, 2015; Dygert et al., 2017; Smye et al., 2017), while ophiolites
88 showing strong subduction influence remain a relatively unexplored field of investigation. Thus, our current
89 knowledge of the cooling mechanisms of subduction-related mantle sequences is scarce.

90 To bridge this gap of knowledge, we have carried out a detailed geothermometric investigation of the New
91 Caledonia ophiolite. This ophiolite constitutes one of the rare examples of a complete forearc sequence
92 originated during subduction inception (Cluzel et al., 2012), thus providing the opportunity to investigate
93 cooling mechanisms in a young forearc section. To unravel the thermal history of the ophiolite, we have applied
94 different chemical thermometers to well-characterized mantle peridotites (lherzolites and harzburgites) from
95 different massifs and to mafic-ultramafic samples (gabbro-norites, wehrlites, pyroxenites, and dunites)
96 belonging to the so-called “cumulitic sequence” of the Massif du Sud. To give a full and representative picture
97 of the thermal evolution of the ophiolite, we have based our study on a robust dataset, including more than

98 eighty samples. Most of the data are compiled from previous geochemical and petrological studies (i.e.
99 Marchesi et al., 2009; Pirard et al., 2013; Secchiari et al., 2016, 2018, 2020; Xu et al., 2020) but new
100 unpublished data were also included.

101 With this study, we aim to: 1) unravel, for the first time, the cooling history and the thermal evolution of an
102 infant proto-arc section; 2) draw new insights into the thermal regime experienced by one of the biggest
103 ophiolitic complexes worldwide; 3) compare our results with data on modern analogues and other ophiolitic
104 sequences worldwide.

105

106 **2 Geological and petrological background**

107 The New Caledonia archipelago lies in the SW Pacific Ocean, between the New Hebrides Arc and the eastern
108 margin of Australia (Figure 1). The main island of New Caledonia (i.e. Grande Terre) constitutes ~ 90% of the
109 land area and is composed of an assemblage of volcanic, sedimentary, and metamorphic terranes, ranging in
110 age from Permian to Miocene (e.g. Aitchison et al., 1995; Cluzel et al., 2001, 2012; Lagabrielle et al., 2013).
111 Pre-Late Cretaceous tectonic events led to the accretion of these terranes onto the eastern Australian margin
112 of Gondwanaland (e.g. Meffre, 1995; Schellart et al., 2006; Whattam, 2009; Cluzel et al., 2012a).

113 Starting from Late Cretaceous, the tectonic evolution of the Southwest Pacific Region included marginal basins
114 opening (i.e. Tasman Sea, New Caledonia, Loyalty/South Loyalty basins) that isolated continental strips of
115 Paleozoic–Jurassic age and renewed island arc formation.

116 The present-day structure of New Caledonia mostly resulted from a Paleogene episode of convergence related
117 to the closure of the South Loyalty basin, which initiated at ~ 56 Ma, (Cluzel et al., 2012a) and gave birth to
118 supra-subduction dykes during the 55-50 Ma interval (Cluzel et al., 2006). Microcontinent-arc collision
119 resulted in the failure of an Eocene NE-dipping subduction (Aitchison et al., 1995; Cluzel et al., 2001, 2012a,
120 2020), culminating in the obduction of the ophiolitic units at ~ 34 Ma (Cluzel et al., 2012b).

121 The samples of this study belong to the “Peridotite Nappe” (Avias, 1967), a large sheet of obducted mantle
122 rocks rooted in the Loyalty basin. Apart from some sparse tectonic klippen, the Peridotite Nappe is mostly
123 exposed in the Massif du Sud, where a ~ 2500 m thick harzburgite–dunite sequence, locally overlain by km-
124 scale lenses of mafic and ultramafic intrusions, crops out. This sequence represents one of the few exposed
125 crust-mantle transects worldwide, generated at the onset of subduction in a nascent arc setting (Marchesi et al.,
126 2009; Pirard et al., 2013; Secchiari et al., 2018). Recent geochemical studies have shown that the dunites and
127 wehrlites have a replacive origin and originated by interaction between a residual mantle sequence and
128 boninitic and arc-tholeiitic magmas (Marchesi et al., 2009; Pirard et al., 2013). Up section, the progressive
129 appearance of orthopyroxene and plagioclase marks the transition to layered dunites, wehrlites/pyroxenites,
130 and, finally, gabbronorites. The layered textures recognized in most gabbronorite outcrops have been ascribed
131 to a cumulitic origin (Marchesi et al., 2009; Pirard et al., 2013; Secchiari et al., 2018). Derivation from magma
132 batches transitional between boninites and tholeiites with a highly depleted trace element signature has been
133 speculated for the gabbronorites (Marchesi et al., 2009; Pirard et al., 2013; Secchiari et al., 2018).

134 Harzburgites are the dominant lithotype of the Peridotite Nappe. They bear an overall refractory composition,
135 testified by exceedingly low contents of incompatible trace elements and the remarkable absence of primary
136 clinopyroxene (Prinzhofer and Allègre 1985; Marchesi et al., 2009; Ulrich et al., 2010; Secchiari et al., 2019,
137 2020). Geochemical studies proposed that the harzburgites acquired their signature through high degrees of
138 fluid-assisted melting above the Eocene subduction zone (~ 20-25%, see Marchesi et al., 2009, Ulrich et al.,
139 2010). More recently, Secchiari and coauthors (2020) proposed that whole rock and orthopyroxene trace
140 element compositions of the harzburgites are consistent with two partial melting episodes in the spinel stability
141 field. A first (undated) melting event likely occurred in a MOR setting and was followed by further melting in
142 a supra-subduction zone environment during the Eocene (Secchiari et al., 2019, 2020) and post-melting
143 metasomatism, resulting in secondary ortho- and clinopyroxene precipitation (Figure S1).

144 Minor spinel and plagioclase-bearing lherzolites (Figure S1) occur in the northernmost part of the island
145 (Ulrich et al., 2010; Secchiari et al. 2016). Unlike the central and southern harzburgitic massifs, the lherzolites
146 do not record a strong subduction fingerprint. Trace element geochemical modelling indicates that their
147 signature could be reproduced by a moderate degree of melt extraction of a depleted mantle source (~ 8-9%),
148 started in the garnet stability field. By contrast, plagioclase lherzolites originated from residual spinel
149 lherzolites through reactive percolation and entrapment of depleted MORB melts in the shallow oceanic
150 lithosphere (Secchiari et al., 2016). As a whole, the petrological and geochemical features displayed by the
151 New Caledonia lherzolites reflect an origin in a spreading ridge environment, possibly a marginal basin
152 predating the Eocene subduction (Secchiari et al., 2016). To date, the relationships between the northern
153 lherzolites and the ultra-depleted harzburgites are difficult to ascertain, based on the available petrological and
154 geochemical data (Ulrich et al., 2010; Secchiari et al., 2020).

155

156 **3 Methods and data sources**

157 To reconstruct the thermal evolution of the New Caledonia ophiolite, geothermometric calculations for a set
158 of eighty-seven samples have been carried out. We report thermometric data for fifty-eight peridotites and
159 twenty-nine mafic and ultramafic intrusives (see Table 1 and 2). Sampled lithologies include: (1) spinel and
160 plagioclase lherzolites from the northern massifs; (2) depleted harzburgites from central and western tectonic
161 klippen and Massif du Sud; (3) mafic and ultramafic rocks from the Massif du Sud, namely cumulitic gabbros,
162 wehrlites, pyroxenites and dunites. The modal compositions of the investigated rock types are reported in Table
163 S1.

164 To calculate equilibrium temperatures, pyroxene, olivine, plagioclase, and spinel major element compositions
165 were taken from the literature (Marchesi et al., 2009; Pirard et al., 2013 ; Secchiari et al., 2016, 2018, 2020 ;
166 Xu et al. 2020). Moreover, to expand the available data, six unpublished analyses (Table 1 and 2) were added
167 to our dataset. For pyroxene and plagioclase trace element contents, we used data from Secchiari et al. (2016,
168 2018).

169 All the data sources analyzed in situ major element composition using a microprobe or a scanning electron
170 microscope (see Table S2 and references for further detail), while pyroxene and plagioclase trace element data

171 (Secchiari et al., 2016, 2018) were measured using laser ablation inductively coupled mass spectrometry (LA-
172 ICP-MS, Table S2).

173 Major element mineral data for the studied samples are reported in Table S3 and Figure S2. Trace element
174 contents of the analyzed minerals and chondrite-normalized REE patterns are reported in Table S4 and Figure
175 2. The mineral phases used in this study display remarkably homogeneous major and trace element
176 compositions, as revealed from the detailed analytical work carried out on these lithologies (see references and
177 Table S2). Significant chemical zoning, for both major and trace elements, is lacking in the mineral phases at
178 the grain size, and intrasample variability appear notably limited (Table S3). Owing to the compositional
179 homogeneity and the excellent analytical quality of the literature data, we believe that the results presented in
180 this work may be representative of the thermal state of the ophiolite. For computing closure temperatures for
181 the various lithologies, average mineral compositions from grain cores were used, in order to avoid possible
182 grain boundaries disturbance. We applied different types of geothermometers: (1) REE-in-two-pyroxene
183 thermometer of Liang et al. (2013), which is based on the composition-dependent temperature sensitivity of
184 REEs+Y exchange between ortho- and clinopyroxene; (2) REE-in-plagioclase–clinopyroxene thermometer
185 (Sun & Liang, 2017), which uses REEs+Y partitioning between coexisting plagioclase and clinopyroxene; (3)
186 two-pyroxene solvus thermometers (Brey and Köhler, 1990; Taylor, 1998), which parameterize temperature-
187 sensitive transfer of the enstatite component between coexisting ortho- and clinopyroxene around the
188 miscibility gap; (4) cation exchange thermometers, based on the temperature sensitivity of intercrystalline
189 exchange of major and trace elements: Ca-in-orthopyroxene, olivine-spinel and Ca-in-olivine thermometers
190 (Brey and Kohler, 1990, Li et al., 1995; De Hoog et al., 2010). In addition, melting temperatures or mantle
191 peridotites were obtained for the lherzolites using the formulation of Lee and Chin (2014).

192 Due to the absence of primary clinopyroxene in the harzburgites, two-pyroxene geothermometers have been
193 applied only to the lherzolites and to some mafic-ultramafic clinopyroxene-bearing intrusives, where the two
194 pyroxenes appeared to be in textural equilibrium. Thus, owing to the depleted nature of the harzburgites, the
195 application of chemical geothermometers is limited to orthopyroxene, olivine, and olivine-spinel based
196 thermometers.

197

198 **4 Results**

199

200 *REE + Y compositions of ortho- and clinopyroxenes used for T calculations*

201

202 Clino- and orthopyroxene from spinel lherzolites have subparallel REE patterns (Figures 2a-b), similar to
203 abyssal-type peridotites (e.g. Johnson et al., 1990; Warren et al., 2009). Slightly higher REE contents are
204 recorded by plagioclase-bearing rocks (Figure 2b). Clinopyroxene displays depleted LREE, relatively flat
205 HREE ($Tb_N/Yb_N = 0.79–1.0$) and MREE/HREE fractionation ($Sm_N/Yb_N = 0.28–0.47$). For some samples, a
206 slight enrichment in La and Ce can be observed. Orthopyroxene from both spinel and plagioclase lherzolites
207 exhibits very depleted compositions, with distinctly lower REE concentrations compared to clinopyroxene,

208 and steeply plunging patterns ($Gd_N/Yb_N = 0.09- 0.15$). Small negative Eu anomalies ($Eu/Eu^* = 0.57- 0.84$)
209 were detected for both clino- and orthopyroxene in plagioclase-bearing lherzolites, due to equilibration with
210 plagioclase.

211 REE concentrations in clinopyroxene from gabbro-norites are strikingly low, with HREE varying between 0.8-
212 2 times chondritic values (Figure 2c). Clinopyroxene REE patterns are characterized by gently sloping profiles,
213 with a progressive increase in concentrations from LREE to HREE ($Ce_N/Yb_N = 0.01- 0.09$) and weakly
214 concave-downward patterns for $Yb_N = 0.93-1.72$. The highly calcic plagioclase (Table S3) also exhibits
215 depleted trace element composition, characterized by flat to slightly enriched LREE, between 0.003 and 0.13
216 times chondrite, and prominent Eu positive anomaly ($Eu/Eu^* = 11- 18$, see Fig. 2d).

217

218 *Temperature inversion*

219

220 As the analyzed minerals do not display significant core-rim compositional variations or intra-sample
221 variability, temperatures were computed using representative average mineral compositions from pyroxene
222 grain cores and cores of clinopyroxene-plagioclase pairs, which generally exhibit low standard deviation
223 values (Table 1, Figure 2). Temperatures were then inverted from the trace element data using the methods
224 discussed in the works of Liang et al. (2013) and Sun and Liang (2017) for the lherzolites and the gabbro-norites,
225 respectively.

226 To assess data quality and consistency for REE-in-two-pyroxene and REE-in-plagioclase-clinopyroxene
227 thermometers, REE abundances were first plotted on chondrite normalized diagrams (Figure 2). Particular
228 attention was devoted to LREE enrichments, which could be a hint of metasomatic processes, and to the
229 smoothness of the REE patterns. Equilibrium conditions between two pyroxenes and plagioclase-
230 clinopyroxene pairs were also evaluated plotting the ratios of the measured REE+Y concentrations in
231 pyroxenes and plagioclase against their ionic radii (Figure 3).

232 REEs-Y data were then plotted for each sample in the inversion diagram, i.e. $\ln(D - A)$ vs. B, where D
233 represents the partition coefficient between ortho- and clinopyroxene or plagioclase and clinopyroxene for
234 REE-in-two-pyroxene and REE-in-plagioclase-clinopyroxene thermometers, and A and B are coefficients
235 determined by major-element compositions and REE ionic radius, respectively (Liang et al., 2013). A line
236 anchored at the origin was then drawn, by fitting the measured data using robust regression method (see Figure
237 S3). The slope of the line is ideally the temperature, and it should overlie all the measured data. In case of
238 scatter from the fitting line, outliers were manually excluded in the reversion analysis and a meaningful
239 temperature was obtained from the linear data. Each sample was carefully examined before being added to or
240 omitted from a database of approved temperatures. Figures generated for the main text of this study only
241 include approved data, which are reported in Tables 1 and 2.

242

243 *Pressure estimates*

244

245 Owing to the lack of geobarometers in garnet- or plagioclase-free systems, a pressure equal to 10 kbar was
 246 assumed for mantle rocks for temperature calculation. A pressure estimate of 10 kbar is reasonable for samples
 247 from both mid-ocean ridge and subduction zones and allows comparison with other literature data.

248 For the mafic-ultramafic sequence, the depth of crystallization was calculated using the FACE geobarometer
 249 (Fumagalli et al., 2017), which relies on the pressure-sensitive equilibrium Forsterite + Anorthite = Ca-
 250 Tschermak + Enstatite. The pressure estimates were obtained for five plagioclase-bearing samples, i.e. three
 251 gabbonorites and two wehrlites (see Table 2), yielding $P = 1.9\text{-}2.8$ kbar and $3.0\text{-}3.2$ kbar, respectively.
 252 Application of the Fumagalli et al. (2017) geobarometer to these lithologies is expected to provide reliable
 253 estimates, as their clinopyroxene X_{Cr} and a_{CaTs} are similar to those of the peridotite samples used to calibrate
 254 the geobarometer (e.g. Basch et al., 2019). When the FACE geobarometer could not be applied, a pressure of
 255 2 kbar was chosen for the gabbonorites, while a slightly higher pressure (i.e. 3 kbar) was assumed for the
 256 wehrlites and the dunites of the cumulitic sequence.

257

258 *T estimates*

259

260 The results of T calculations are summarized in Tables 1-3.

261 REE-in-two-pyroxene geothermometer (T_{REE-Y} , i.e. Liang et al., 2013) for the spinel lherzolites provide
 262 temperatures ranging between $1256\text{-}1334$ °C (Table 1), with the highest T_{REE-Y} recorded by plagioclase
 263 lherzolites ($1314\text{-}1394$ °C).

264 T_{REE-Y} are not available for the mafic-ultramafic intrusives, as petrographic observations (e.g. Secchiari et al.,
 265 2018) and inversion diagrams (i.e. $\ln(D-A)$ vs. B, Liang et al., 2003; Dygert and Liang, 2015) indicate
 266 disequilibrium between the two pyroxenes. The disequilibrium state is also attested by the calculated opx/cpx
 267 partition coefficients, which significantly deviate from modeling trends (e.g. Lee et al., 2007, see Figures 3).
 268 For the gabbonorites, we have applied REE-in-plagioclase-clinopyroxene thermometer (T_{Pl-Cpx} , i.e. Sun and
 269 Liang, 2017) after assessing plagioclase-clinopyroxene equilibrium. High-temperature values ($1241\text{-}1243$ °C)
 270 were obtained for two samples (PL1, PR3). Despite the REE-Y pattern of PR3 gabbonorite appears a bit
 271 disturbed in Figure 3, we decided to keep T_{Pl-Cpx} for this sample, as temperature inversion diagrams attest
 272 plagioclase-clinopyroxene equilibrium (Figure S3). Likewise, the calculated T_{Pl-Cpx} is remarkably similar to
 273 PL1 gabbonorite, suggesting that the REE-Y pattern in Figure 3 may rather reflect the low trace element
 274 concentrations.

275 For the lherzolites, the exchange of Ca-Mg between pyroxenes (T_{BKN} , i.e. Brey and Köhler, 1990; T_{Ta} , i.e.
 276 Taylor, 1998) records much lower temperatures compared to the T_{REE} thermometer (average $\Delta T \sim 300$ °C),
 277 consistent with previous data on modern and ophiolitic peridotites from MOR setting (Liang et al., 2013;
 278 Dygert and Liang, 2015; Dygert et al., 2017). T_{BKN} and T_{Ta} yield large and comparable temperature intervals
 279 for the lherzolites ($T_{BKN} = 776\text{-}993$ °C; $T_{Ta} = 758\text{-}1026$ °C), with the lowest temperatures registered by BAB2B
 280 sample. By contrast, T_{BKN} obtained for the mafic and ultramafic intrusives (Table 2 and 3) are indicative of
 281 higher equilibrium temperatures ($T_{BKN} = 964\text{-}1083$ °C; $T_{Ta} = 942\text{-}1092$ °C).

282 Among cation exchange thermometers, Ca-in-orthopyroxene ($T_{\text{Ca-in-Opx}}$, i.e. Brey and Köhler, 1990) records
 283 the highest temperatures for the peridotites (Iherzolites: $T_{\text{Ca-in-Opx}} = 1010\text{-}1082$ °C; harzburgites: $T_{\text{Ca-in-Opx}} =$
 284 $903\text{-}1185$ °C). Ca-in-olivine ($T_{\text{Ca-in-Ol}}$, i.e. De Hoog et al., 2006) and olivine-spinel Fe-Mg thermometer ($T_{\text{Ol-Sp}}$,
 285 i.e. Li et al., 1995) indicate similar equilibrium temperatures for the peridotites (Iherzolites: $T_{\text{Ca-in-Ol}} = 824\text{-}$
 286 893 °C, $T_{\text{Ol-Sp}} = 794 - 950$ °C; harzburgites: $T_{\text{Ca-in-Ol}} = 741\text{-}938$ °C, $T_{\text{Ol-Sp}} = 815\text{-}1007$ °C).

287 For the mafic-ultramafic sequence, $T_{\text{Ca-in-Opx}}$ varies between $889\text{-}1147$ °C (see Table 2 and 3), with temperatures
 288 shifted toward slightly higher values in the ultramafic lithologies (average $T_{\text{Ca-in-Opx}} = 1064$ °C) with respect to
 289 the gabbro-norites (1021 °C). Lower temperatures are provided by Ca-in-olivine and olivine-spinel Fe-Mg
 290 thermometers ($T_{\text{Ca-in-Ol}} = 684\text{-}899$ °C; $T_{\text{Ol-Sp}} = 839\text{-}982$ °C, see Table 2 and 3)

291 Calculated $T_{\text{REE-Y}}$ were plotted against T_{BKN} , $T_{\text{Ca-in-Opx}}$ and $T_{\text{Ol-Sp}}$ for the Iherzolites (Figures 4a-c). In the
 292 variation diagrams, the Iherzolites invariably plot far above the 1:1 line, partially overlapping the field of
 293 abyssal peridotites and the hottest ophiolitic peridotites. Plagioclase-bearing lithologies appear hotter on
 294 average, falling outside the field of the abyssal peridotites. The relationships occurring between T_{REE} and
 295 mineral composition are illustrated in Figure S4. No correlation can be observed between T_{REE} and the fertility
 296 indicators, i.e. olivine Mg# or spinel Cr# (Figures S4a-b), in agreement with previous observations on mantle
 297 peridotites (Dygert and Liang, 2015; Dygert et al., 2017).

298 By contrast, a weak positive correlation is displayed by T_{REE} and orthopyroxene Ca contents (Figure S3c),
 299 possibly reflecting temperature-sensitive Ca partitioning around the enstatite-diopside solvus.

300

301 **5 Discussion**

302

303 **5.1 Origin and cooling history of the northern peridotite massifs**

304

305 Spinel- and plagioclase-bearing Iherzolites from New Caledonia provide comparable equilibration
 306 temperatures, suggesting similar cooling histories (see Table 1).

307 The Iherzolites from Poum and Babouillat yield some of the highest $T_{\text{REE-Y}}$ ever reported for ophiolites and
 308 abyssal peridotites (e.g. Dygert and Liang, 2015). Among the studied samples, the highest $T_{\text{REE-Y}}$ (up to ~
 309 1400 °C) were recorded by two plagioclase-bearing lithologies (BAB2A-BAB2B). Similar high temperatures
 310 are often registered by plagioclase-impregnated peridotites. The anomalously high T have been tentatively
 311 attributed to REE+Y disequilibrium partitioning between the two pyroxenes, due to reactive melt percolation
 312 (Liang et al., 2013; Dygert and Liang, 2015).

313 To quantify the cooling rates experienced by the studied rock types, we have applied the method of Dygert
 314 and Liang (2015) and Dygert et al. (2017). Figure 4d illustrates closure curves built using a modified form of
 315 Dodson's equation (Ganguly & Tirone, 1999), which models the dependence of closure temperature (T_c) on
 316 grain size, initial temperature, and cooling rate, assuming the closure of T_{REE} are rate-limited by diffusion of
 317 REEs in orthopyroxene (Cherniak & Dimanov, 2010) and the closure of T_{BKN} are approximated by diffusion
 318 of Fe–Mg in clinopyroxene (Dimanov & Wiedenbeck, 2006). Red lines in Figure 4d represent cooling curves

319 for one-stage cooling starting at peak temperature (T_0), presumably along the solidus, to final closure
320 temperatures for T_{REE} and T_{BKN} , depending on cooling rate (vertical black lines). Cooling curves have been
321 calculated for a grain radius of 2.5 mm, i.e. the average grain size obtained through petrographic observations.
322 In Figure 4d, BA1, BAB1B and POU2 lherzolite samples plot in a region typical of abyssal peridotites and
323 mid-ocean ridge ophiolites (such as Corsica and Oman, e.g. Dygert et al. 2017), whereas the other plagioclase
324 lherzolites (BAB2A, BAB2B and POU1A) fall outside the cooling curves, lying at the top left. Samples falling
325 in this area in cooling diagrams are believed to reflect thermal disturbance related to melt-rock reactions or
326 complex thermal histories (i.e. early cooling followed by re-heating, e.g. Dygert and Liang, 2015; Dygert et
327 al., 2017). Thus, these temperatures cannot be considered as representative of the thermal state of the lherzolite
328 massifs.

329 Results for BA1, BAB1B and POU2 samples are consistent with cooling from asthenospheric temperatures of
330 1400°C and 1300°C, respectively, at cooling rates of $\approx 4 \times 10^{-3}$ °C/yr. These cooling rates are similar to those
331 registered by other ophiolitic mantle sections (i.e. Dygert and Liang, 2015; McGoldrick et al., 2018; Canil et
332 al., 2019), but slightly higher compared to those reported for SSZ peridotites ($\sim 10^{-6}$ - 10^{-4} , see Dygert and Liang,
333 2015). Intriguingly, these values tend to be somewhat lower compared to the cooling rates registered by the
334 Wadi Tayin mantle (i.e. Oman, see Dygert et al., 2017), which is overlapped by a 5-7 km thick crustal sequence.
335 This observation supports the suggestion of Dygert et al. (2017) that cooling of the oceanic mantle is not
336 governed by the thickness of overlying crust in any systematic way.

337 The cooling rates deduced for the New Caledonia lherzolites also cover the same range of values of the oceanic
338 lower crustal lithosphere dominated by conductive cooling (e.g. Coogan et al., 2002; Faak & Gillis, 2016;
339 Dygert et al., 2017), in contrast to lithospheric sections re-equilibrated through hydrothermal circulation, which
340 generally yield cooling rates one or two orders of magnitude higher ($\approx 10^{-2}$ or 10^{-1} , e.g. VanTongeren et al.,
341 2008; Dygert et al., 2017).

342 For spinel lherzolites BA1 and POU2, melting temperatures were also computed using the method proposed
343 by Lee and Chin (2014), which is based on bulk MgO, FeO_t, and SiO₂ contents. Temperatures for anhydrous
344 melting are in good agreement with peak temperatures obtained with the method of Dygert and Liang (2015)
345 for spinel lherzolites ($T = 1383^\circ\text{C}$ for BA1 and $T = 1410^\circ\text{C}$ for POU2), lying in the range of most abyssal
346 peridotites (Lee and Chin, 2014).

347 Temperatures calculated with other geothermometers exhibit a smooth and systematic decrease in the order:
348 $T_{\text{Ca-in-Opx}}$, T_{Ta} and T_{BKN} , $T_{\text{Ol-Sp}}$ and $T_{\text{Ca-in-Ol}}$. This systematic decrease can be related to the different diffusion
349 rates of the various elements (or components) used to calibrate the thermometers (Chakraborty, 2010; Cherniak
350 and Dimanov, 2010).

351 Major element-based thermometers for Poum and Babouillat lherzolites record temperatures in the range of
352 abyssal and ophiolitic peridotites from MOR setting (Table 1, Figure 5), similar to $T_{\text{REE-Y}}$ estimates.

353 To assess how cooling proceeds at lower temperature conditions, cooling rates from Ca-in-olivine thermometry
354 were computed for the investigated samples assuming an average grain radius of 1 mm, as indicated from
355 petrographic investigations. The calculated values provide consistent results for all the lherzolites, in the range

356 of $\approx 10^{-3}$ °C/y. Remarkably, these cooling rates are comparable to those recorded by $T_{\text{REE-Y}}$ and T_{BKN} at higher
 357 temperature intervals.

358 We propose that the similarities between the abyssal peridotites and the New Caledonia lherzolites mirror an
 359 evolution in a marginal basin predating Eocene subduction, followed by fast uplift and emplacement. Such
 360 fast emplacement possibly occurred along a transform fault (Prinzhofer & Nicolas, 1980; Titus et al., 2011),
 361 in agreement to what was previously proposed by Secchiari et al., (2016) based on the melting history of the
 362 lherzolites. Notably, the presence of a major shear zone, running along the northeastern side of the Belep
 363 Islands and Poum and Tiebaghi massifs, has been reported for many years by Nicolas (1989), who interpreted
 364 this high-strain zone as a paleo-transform fault (Nicolas, 1989).

365 The similar cooling rates, in the range of 10^{-3} °C/y, recorded through the high and lower temperature intervals
 366 also suggest that cooling and thermal re-equilibration must have continued at constant rates throughout the
 367 whole post-melting evolution of the lherzolite massif, and possibly by conduction.

368

369 **5.2 Thermal evolution of the ultra-depleted harzburgites**

370

371 Due to the lack of primary clinopyroxene, high-temperature constraints for the New Caledonia harzburgites
 372 are difficult to obtain.

373 Despite the fact that two pyroxene exchange thermometers cannot be applied to constrain cooling of the
 374 harzburgites from peak temperature, temperature estimates can still be obtained using orthopyroxene major
 375 element compositions. These values represent minimum temperatures under the assumption that
 376 orthopyroxene composition reflects equilibrium with clinopyroxene. This appears reasonable, as cooling of an
 377 initially clinopyroxene-undersaturated orthopyroxene and subsolidus exchange of Ca with olivine will result
 378 in clinopyroxene saturation (Lindsley, 1983). Notably, clinopyroxene exsolution lamellae are widely observed
 379 within porphyroclastic orthopyroxene in the analysed harzburgites. As a whole, $T_{\text{Ca-in-Opx}}$ computed for the
 380 investigated samples are relatively high and homogeneous, giving an average $T_{\text{Ca-in-Opx}} = 1020$ °C. The
 381 calculated range of values ($T_{\text{Ca-in-Opx}} = 903\text{--}1185$ °C) appear wider and shifted towards slightly higher values
 382 than temperatures reported by Pirard and coauthors (2013) for the same lithologies ($T_{\text{Ca-in-Opx}} = 953\text{--}970$ °C),
 383 falling in the range of abyssal and other subduction-related peridotites (Dygert and Liang, 2015; Dygert et al.,
 384 2017). Notably, the lower temperature interval (903–923 °C) is mainly covered by the mylonitic harzburgites
 385 from the Ouassè bay (Table 1). Such low temperatures are likely related to deformation along the Bogota shear
 386 zone (Titus et al., 2011), which produced mylonitic textures and overall grain size reduction. Alternatively,
 387 the lower temperatures preserved by these harzburgites may reflect a shear heating temperature, overwriting
 388 the previous thermal history. For the Bogota mylonites, the occurrence of orthopyroxene neoblasts providing
 389 equilibrium temperatures similar to the coexisting porphyroclasts ($T_{\text{Ca-in-Opx}} = 923\text{--}945$ °C, Secchiari et al.,
 390 unpublished data) supports the hypothesis that thermal re-equilibration of orthopyroxene porphyroclasts
 391 occurred after shearing and grain size reduction. Further constraints on the subsolidus thermal evolution of the
 392 harzburgites are provided by Ca in olivine ($T_{\text{Ca-in-Ol}}$) and olivine-spinel geothermometers ($T_{\text{Ol-Sp}}$). As these

393 thermometers are based on the exchange of relatively fast-diffusing mineral components, their application
394 offers crucial insights on the last cooling stages of mantle peridotites, as well as on the emplacement
395 mechanisms of the peridotite massifs. In particular, the equilibrium exchange of Mg^{2+} and Fe^{2+} between olivine
396 and spinel represents the fastest exchange and continues during cooling down to relatively low temperatures
397 (~ 500 °C, e.g. Fabriès, 1979). Hence, the olivine-spinel geothermometer yields the temperatures of the last
398 stages of equilibration, when an equilibrium state is almost reached or exchange reactions are blocked by
399 cooling.

400 Temperatures calculated with $T_{Ca-in-Ol}$ thermometer for the New Caledonia harzburgites cover a wide range of
401 values (741-938 °C, average $T_{Ca-in-Ol} = 842$ °C, see Table 1 and 3), mirroring the variable Ca contents of olivine
402 (Table S3).

403 Olivine-spinel geothermometer records even higher temperatures compared to Ca-in-olivine thermometer,
404 bearing values up to 1000 °C, with an average of $T_{Ol-Sp} = 924$ °C. As a whole, the harzburgites exhibit
405 remarkably higher equilibrium temperatures for the fast diffusing thermometers (Fig. 5) in comparison to all
406 ophiolitic - both from supra-subduction zone and MOR setting - and modern arc peridotites, plotting in the
407 field of modern abyssal mantle. This observation represents an interesting contrast with the previous results
408 on obducted ophiolitic peridotites (e.g. Hanghøj et al., 2010; Dygert et al., 2017), for which slower cooling
409 than abyssal peridotites is generally observed (Dygert et al., 2017; Canil et al., 2019), possibly as a result of
410 hydrothermal cooling cessation after obduction.

411 To gain additional insights into the thermal history of the harzburgites, we computed cooling rates using Ca-
412 in-olivine thermometer. For this calculation, we used an olivine grain radius of 0.8 mm for the harzburgites
413 from the central peridotite massifs, while 1 mm radius was chosen for the sample from Yaté (YA1), based on
414 petrographic observations. For the other samples from literature, a grain radius of 1 mm was assumed. This
415 approximation is reasonable, as most of the studied harzburgites were sampled in the Massif du Sud area, close
416 to our YA1 sample. The calculated cooling rates yield similar values for all the investigated harzburgites, in
417 the range of $10^{-4} - 10^{-3}$ °C/y. These results are comparable with those obtained for the northern Iherzolites,
418 falling in the range of the oceanic lithosphere that cooled via conduction (e.g. Coogan et al., 2002).

419 Previous studies have shown that, among mantle rocks, forearc peridotites generally register the lowest
420 equilibration temperatures (Parkinson & Pearce, 1998; Ohara and Ishii, 1998; Zanetti et al., 2006) . These
421 thermal features were interpreted to reflect long cooling histories, dominated by low heat extraction rates, in
422 presence of water (e.g. Dygert and Liang, 2015).

423 In order to unveil the meaning of the atypical thermal state recorded by the investigated lithotypes, the
424 geodynamic evolution of the New Caledonia archipelago needs to be taken into account. Geodynamic models
425 indicate that New Caledonia experienced a phase of marginal basin formation starting from Campanian to
426 Paleocene, followed by intra-oceanic subduction during Eocene (~ 56 Ma, Cluzel et al., 2016). It has been
427 proposed that the Eocene subduction started close to or in correspondence of an active oceanic spreading center
428 (Ulrich et al., 2010), where relatively hot and young lithosphere ($\approx 6-9$ Ma old, see Cluzel et al. 2016) was
429 forced to subduct. Continued convergence finally resulted in proto arc-continent collision, which led to

430 overthrusting of the ophiolitic units onto the Norfolk ridge ~ 34 Ma ago (Cluzel et al., 2012 b). In this
431 framework, the results provided by the fast diffusing thermometers may be explained as reflecting short
432 residence times of the depleted mantle from the forearc region (~ 20 Ma), followed by fast emplacement due
433 to obduction (Aitchison et al., 1995; Cluzel et al., 2012 a, b; Lagabrielle et al., 2013).

434 This conclusion challenges the general assumption that subduction-related peridotites cool over longer time
435 intervals and possibly from lower initial temperatures (Dyger and Liang, 2015). We interpret this apparent
436 contradiction as specifically related to the tectonic evolution of the New Caledonia archipelago, i.e. to the
437 development of an ephemeral subduction system involving a young oceanic lithosphere. Notably, the young
438 age of the subducted lithosphere is also expected to have prevented the presence of large volumes of sediments
439 and fluids in the subduction zone (Cluzel et al., 2016; Secchiari et al., 2020).

440

441 **5.3 Genesis and cooling mechanisms of the mafic-ultramafic sequence**

442

443 The mineralogical variability of the New Caledonia layered mafic and ultramafic intrusives, allowed the
444 application of several geothermometers.

445 In the uppermost part of the intrusive sequence, T estimates based on the REE-Y exchange between plagioclase
446 and clinopyroxene ($T_{\text{Pl-Cpx}}$, Sun and Liang, 2017) yield high values (1241-1243 °C), which are interpreted as
447 crystallization temperatures of the gabbronorite parental melts (see also Secchiari et al., 2018). Previous studies
448 hypothesized that the gabbronorite crystallization occurred at low-pressure conditions (~ 2-4 kbar, i.e. Pirard
449 et al., 2013). These values are in good agreement with our estimates obtained using the FACE geobarometer
450 (~ 2-3 kbar). The inferred depths are remarkably low compared to the crust-mantle transition of exposed arc
451 sections (e.g. P ~ 10 kbar for Kohistan, Burg et al., 1998) and are consistent with magma emplacement in a
452 thinned forearc lithosphere during subduction initiation (see also Pirard et al., 2013). Derivation from boninitic
453 magmas was previously proposed for the New Caledonia gabbronorites (Marchesi et al., 2009; Pirard et al.,
454 2013). However, their ultra-depleted compositions, coupled with the early appearance of plagioclase and late
455 segregation of orthopyroxene, point to crystallization from H₂O-poor magmas more akin to tholeiites. More
456 specifically, the composition of the parental melts in equilibrium with the New Caledonia gabbronorites was
457 shown to significantly diverge from boninitic melts in having lower LREE-MREE (i.e. light and medium rare
458 earth elements) and FME (i.e. fluid mobile elements) contents, no Nb depletion, and in the lack of Zr -Hf
459 positive anomalies (Secchiari et al., 2018). Notably, $T_{\text{Pl-Cpx}}$ (Sun and Liang 2017) obtained in this study appear
460 ~ 150 °C lower than temperatures experimentally determined by Falloon and Danyushevsky (2000) for
461 boninitic melts.

462 Other insights concerning the thermal evolution of the gabbronorites can be obtained from Ca-in-Opx and two
463 pyroxene Fe-Mg thermometers. $T_{\text{Ca-in-Opx}}$ (925-1110 °C; average $T_{\text{Ca-in-Opx}} = 1021$ °C) mainly fall in the range
464 of the two-pyroxene thermometer estimates (see Table 3). As a whole, pyroxene thermometry give
465 considerably lower temperatures compared to $T_{\text{Pl-Cpx}}$ ($\Delta T \sim 200$ °C), which can be ascribed to higher diffusion

466 rates of divalent cations with respect to trivalent REE. $T_{\text{Ca-in-Opx}}$ and two pyroxene Fe-Mg thermometers thus
 467 depict the subsolidus evolution of the gabbronorites.

468 Major element pyroxene thermometry was also applied to the ultramafic rocks from the base of the layered
 469 intrusive lenses of the New Caledonia ophiolite (i.e. wehrlites, pyroxenites and some dunites, see Tables 2-3).
 470 For these rock types, the calculated $T_{\text{Ca-in-Opx}}$ and T_{BKN} provide similar values to the overlying gabbronorites,
 471 with an average 1064 °C and 1023 °C, respectively (Table 3).

472 On the other hand, an upward decrease of $T_{\text{Ca-in-OI}}$ is recorded from the wehrlites (796-899 °C, average $T_{\text{Ca-in-OI}}$
 473 = 850 °C) and the gabbronorites (684–819 °C, average $T_{\text{Ca-in-OI}}$ = 732 °C), mirroring the higher Ca contents of
 474 the ultramafic rocks (up to \approx 500 ppm for the wehrlites, see Table S3). By contrast, the extreme Ca contents
 475 shown by the dunites (up to 1800 ppm, see Table S3), possibly reflect the lack of sub-solidus equilibrium,
 476 owing to the absence of pyroxene (Pirard et al., 2013). Thus, $T_{\text{Ca-in-OI}}$ for the dunites cannot be assumed as
 477 representative of their cooling state and were not considered. Information on the subsolidus history of the
 478 dunites can only be obtained using the olivine-spinel geothermometer, which records similar temperatures
 479 compared to the other ultramafic lithologies (average $T_{\text{OI-Sp}}$ = 906 °C and 888 °C for the dunites and wehrlites-
 480 pyroxenites, respectively) and to the only spl-bearing gabbronorite sample included in our dataset ($T_{\text{OI-Sp}}$ = 866
 481 °C). As a whole, $T_{\text{Ca-in-OI}}$ and $T_{\text{OI-Sp}}$ are high and homogeneous for the mafic-ultramafic cumulates, falling in
 482 the range of the New Caledonia harzburgites and abyssal peridotites (Fig. 5).

483 To better constrain the thermal history of the mafic-ultramafic sequence, olivine cooling rates were also
 484 computed for the gabbronorites and the wehrlites. An olivine grain radius of 0.5 mm was used for the
 485 gabbronorites from the work of Secchiari et al., (2018). The same grain size was assumed for the gabbronorites
 486 and Opx-gabbros from literature, while we chose an olivine grain size of 0.8 mm for the wehrlites, as
 487 petrographic observations generally revealed a coarser grain size for these lithotypes. Our results indicate
 488 cooling rates of $\approx 10^{-4}$ °C/y for the gabbronorites (except PR1B sample, which shows a higher cooling rate, \approx
 489 10^{-3}) and 10^{-3} °C/y for the wehrlites (Table 2). One gabbronorite sample (MDS37) exhibits remarkably higher
 490 cooling rates ($\approx 10^{-2}$ °C/y) compared to the other mafic-ultramafic rocks in our dataset. However, this value is
 491 several orders of magnitude higher compared to the other gabbronorites from the same locality. Thus, we
 492 believe that this high value possibly derived from a wrong assumption of the olivine grain size, rather than
 493 being representative of the real cooling rate experienced by the gabbronorites.

494 To assess temperature variations with depth across the Massif du Sud sequence, average closure temperatures
 495 for each geothermometer were reported for the mafic-ultramafic cumulates and the underlying tectonite
 496 harzburgite (Fig. 6). This allows us to build, even if in a qualitative way, temperature profiles from the lower
 497 crust to the mantle, passing through the Moho transition zone. As it can be observed, temperature variation
 498 with depth appears limited, with the various geothermometers mostly showing high and constant temperatures
 499 moving from the lower crust (i.e. the gabbronorites) to the depleted peridotite. Likewise, the cooling rates
 500 estimated from Ca-in-olivine thermometer mirror the trend shown by the various geothermometers, displaying
 501 limited variations from the lower crust to the tectonite harzburgite.

502 Recent geochemical works proposed that the New Caledonia mafic-ultramafic sequence originated in a nascent
 503 intra-oceanic arc, from multiple, non-cogenetic, magma batches bearing a depleted supra-subduction zone
 504 signature (Marchesi et al., 2009; Pirard et al., 2013; Secchiari et al., 2018). From this perspective, we are prone
 505 to interpret our results as reflecting the emplacement of hot, depleted magma batches in a young forearc
 506 lithosphere, as supported by the high T_{Pl-Cpx} , followed by cooling and sub-solidus re-equilibration.

507 The similar thermal conditions and cooling rates hint that the mafic-ultramafic sequence, together with the
 508 depleted forearc mantle, experienced a similar history of cooling and thermal re-equilibration at lower
 509 temperatures. In particular, the high equilibrium temperatures computed with the fast diffusing
 510 geothermometers, in the range of modern abyssal peridotites, are atypical in a forearc region and strikingly
 511 contrast with the previous results for this geodynamic setting. The thermal signature preserved by the New
 512 Caledonia ophiolite likely reflects its geodynamic evolution, i.e. to the development of an ephemeral
 513 subduction, suddenly followed by obduction and emplacement of the ophiolitic units (Cluzel et al., 2012).

514 For the Ca-in-olivine thermometer, slightly lower equilibrium temperatures, coupled to lower olivine cooling
 515 rates, are recorded by some gabbro-norites compared to the underlying wehrlites. However, these variations
 516 appear limited and were possibly related to disturbance of the Ca-in-olivine thermometer, perhaps due to re-
 517 heating beyond Ca in olivine closure temperature.

518 Unfortunately, the lack of geothermometric studies carried out in complete sequences from forearc setting
 519 prevents any comparison with similar crust-mantle transects (Dygert et al., 2015). This can be reconciled with
 520 the rare occurrence of complete forearc sections in ophiolites (e.g. Greene, 2006; Garrido et al., 2007), as well
 521 as the difficulty in accessing complete crustal sequences in modern forearc environments.

522

523

524 **6 Summary and concluding remarks**

525

526 In this work, we present the first detailed geothermometric investigation carried out in a young forearc
 527 sequence originated during subduction inception. To unravel how the oceanic lithosphere cools in this poorly
 528 investigated geodynamic setting, various chemical thermometers (i.e. T_{REE-Y} , $T_{Ca-in-Opx}$, T_{BKN} , $T_{Ca-in-Ol}$, T_{Ol-Sp} ,
 529 T_{Pl-Cpx}) were applied to peridotite and mafic-ultramafic cumulates from the New Caledonia ophiolite. Cooling
 530 rates, using combined T_{REE-Y} and T_{BKN} and $T_{Ca-in-Ol}$, were also computed.

531 Equilibrium temperatures calculated for the lherzolites indicate that spinel- and plagioclase-bearing lithologies
 532 experienced similar thermal histories. T_{REE-Y} computed for the lherzolites from Poum and Babouillat areas are
 533 among the highest ever documented for ophiolitic peridotites (1256–1334 °C), falling in the range of modern
 534 abyssal peridotites. By contrast, temperatures up to 1400 °C were attested for some of the plagioclase
 535 lherzolites of our dataset. These elevated values can be explained as related to pyroxene disequilibrium and
 536 reactive melt percolation. Closure temperatures models (T_{BKN} vs T_{REE}) indicate that the lherzolites underwent
 537 cooling from asthenospheric temperatures at cooling rates of approximately 4×10^{-3} °C/yr, similar to the
 538 oceanic lower crustal lithosphere re-equilibrated through conduction. Similar values ($\approx 10^{-3}$ °C/yr) were

539 obtained through Ca in olivine geospeedometer, indicating that cooling rates did not change significantly at
540 lower temperatures.

541 Temperatures provided by other chemical geothermometers for the lherzolites are also high, covering the range
542 of abyssal peridotites. As a whole, these features may be tentatively ascribed to post-melting evolution and
543 exhumation along a transform fault, in a marginal basin predating Eocene subduction.

544 Highly refractory, cpx-free, harzburgites constitute the dominant lithology in the New Caledonia ophiolite.
545 These rock types preserve evidence of a high-T evolution testified by $T_{\text{Ca-in-Opx}}$, $T_{\text{Ca-in-Ol}}$ and $T_{\text{Ol-Sp}}$, in turn, give
546 relatively high values, similar to modern abyssal peridotites. Cooling rates computed with Ca in olivine
547 thermometer yield values $\approx 10^{-3}$ °C/yr. These observations contrast with previous results obtained on ophiolitic
548 peridotites, which generally display lower equilibrium temperatures and cooling rates compared to modern
549 oceanic peridotites. Remarkably, such thermal evolution is also unexpected in forearc mantle sections, where
550 cooling is thought to take place starting from lower initial temperatures and at slower cooling rates. This
551 apparent contradiction may be reconciled with the development of an ephemeral subduction event during
552 Eocene, followed by forearc exhumation and emplacement of the Peridotite Nappe via obduction.

553 Similar thermal conditions are also recorded by the mafic-ultramafic sequence. The gabbronorites register high
554 $T_{\text{Pl-Cpx}}$, consistent with their derivation from primitive, H₂O-poor magmas, transitional towards tholeiites.
555 Major element-based thermometers bear high and constant equilibrium temperatures for the mafic and
556 ultramafic lithologies. Likewise, temperature profiles across the Massif du Sud sequence point to limited
557 temperature variations with depth, i.e. from the lower crust to the forearc mantle peridotite. Likewise, Ca in
558 olivine geospeedometer indicate similar cooling rates with depth, in the order of $\approx 10^{-4}$ - 10^{-3} °C/y.

559 These results are consistent with ascent and injection of non-cogenetic magma batches in a young forearc
560 lithosphere during the early stages of the Eocene subduction, followed by cooling and equilibration at lower T
561 due to obduction.

562 Our study illustrates how geothermometric investigation of supra-subduction zone ophiolitic complexes can
563 provide crucial insights to unravel the thermal evolution and cooling history of the lithosphere in nascent arc
564 settings. In particular, our results show for the first time that the thermal conditions preserved by forearc
565 lithosphere are only partly inherited from the tectonic setting. Temperature profiles also appear intimately
566 linked to specific geological processes of the investigated area, as well as to the previous lithosphere evolution.
567 Detailed sampling of the different forearc layers and thorough knowledge of the studied area (geology,
568 tectonics etc...) are hence pivotal to unravel the thermal history of such sequences.

569 We hope that our work motivates further investigation of the New Caledonia ophiolite, possibly combining
570 geothermometric data and geodynamic modeling, to gain new insights into the post-melting evolution,
571 emplacement and obduction of the Peridotite Nappe.

572

573 **Acknowledgements**

574

575 This study has been supported by Italian-PRIN 2017-KY5ZX8. This work has also benefited from the
576 equipment and framework of the COMP-HUB Initiative, funded by the ‘Departments of Excellence’ program
577 of the Italian Ministry for Education, University and Research (MIUR, 2018-2022). In particular, we wish to
578 thank Andrea Comelli for thin section preparation and Luca Barchi for support during SEM-EDS analyses.
579 We also thank J. Blichert-Toft for editorial handling. Constructive reviews by Nick Dygert, Alessio Sanfilippo,
580 John Shervais, and an anonymous reviewer are greatly acknowledged.

581

582 **Data Availability Statement**

583

584 The data used in this study are included as Tables in the supporting information. They are also available in a
585 public data repository at <https://doi.org/10.5281/zenodo.5676145>

586

587 **References**

588

- 589 Aitchison, J. C., Clarke, L., Meffre, S., & Cluzel, D. (1995). Eocene arc-continent collision in New
590 Caledonia and implications for regional Southwest Pacific tectonic evolution. *Geology*, *23*(2), 161–164.
- 591 Aldanmaz, E. (2012). Trace element geochemistry of primary mantle minerals in spinel-peridotites from
592 polygenetic MOR-SSZ suites of SW Turkey: constraints from an LA-ICP-MS study and implications
593 for mantle metasomatism. *Geological Journal*, *47*(1), 59–76. <https://doi.org/10.1002/gj.1336>
- 594 Avias, J. (1967). Overthrust structure of the main ultrabasic new caledonian massives. *Tectonophysics*, *4*(4–
595 6), 531–541.
- 596 Barth, M. G. (2003). Geochemistry of the Othris Ophiolite, Greece: Evidence for Refertilization? *Journal of*
597 *Petrology*, *44*(10), 1759–1785. <https://doi.org/10.1093/petrology/egg058>
- 598 Basch, V., Borghini, G., Fumagalli, P., Rampone, E., Ferrando, C., Gandolfo, A. (2019). Plagioclase-facies
599 thermobarometric evolution of the External Liguride pyroxenite-bearing mantle (Suvero, Italy). *Ophioliti*,
600 *45*(1), 1–11.
- 601 Batanova, V. G., Belousov, I. A., Savelieva, G. N., & Sobolev, A. V. (2011). Consequences of Channelized
602 and Diffuse Melt Transport in Supra-subduction Zone Mantle: Evidence from the Voykar Ophiolite
603 (Polar Urals). *Journal of Petrology*, *52*(12), 2483–2521. <https://doi.org/10.1093/petrology/egr053>
- 604 Brey, G. P. & Köhler, T. (1990). Geothermobarometry in four-phase lherzolites II. New thermobarometers,
605 and practical assessment of existing thermobarometers. *Journal of Petrology*, *31*(6), 1353–1378.
- 606 Canil, D., Grundy, R., & Johnston, S. T. (2019). Thermal history of the Donjek harzburgite massif in
607 ophiolite from Yukon, Canada with implications for the cooling of oceanic mantle lithosphere. *Lithos*,
608 *328–329*, 33–42. <https://doi.org/10.1016/j.lithos.2019.01.001>
- 609 Chakraborty, S. (2010). Diffusion coefficients in olivine, wadsleyite and ringwoodite. *Reviews in Mineralogy*
610 *and Geochemistry*, *72*(1), 603–639. <https://doi.org/10.2138/rmg.2010.72.13>
- 611 Cherniak, D. J., & Dimanov, A. (2010). Diffusion in pyroxene, mica and amphibole. *Reviews in Mineralogy*

- 612 *and Geochemistry*, 72(1), 641–690. <https://doi.org/10.2138/rmg.2010.72.14>
- 613 Cluzel, Dominique, Maurizot, P., Collot, J., & Sevin, B. (2012). An outline of the Geology of New
 614 Caledonia ; from Permian – Mesozoic Southeast Gondwanaland active margin to Cenozoic obduction
 615 and supergene evolution. *Episodes*, 35(1), 72–86. <https://doi.org/10.1029/2004TC001709>
- 616 Cluzel, Dominique, Aitchison, J. C., & Picard, C. (2001). Tectonic accretion and underplating of mafic
 617 terranes in the Late Eocene intraoceanic fore-arc of New Caledonia (Southwest Pacific): geodynamic
 618 implications. *Tectonophysics*, 340(1–2), 23–59. [https://doi.org/10.1016/S0040-1951\(01\)00148-2](https://doi.org/10.1016/S0040-1951(01)00148-2)
- 619 Cluzel, Dominique, Meffre, S., Maurizot, P., & Crawford, A. J. (2006). Earliest Eocene (53 Ma)
 620 convergence in the Southwest Pacific; evidence from pre- obduction dikes in the ophiolite of New
 621 Caledonia. *Terra Nova*, 18(6), 395–402. <https://doi.org/10.1111/j.1365-3121.2006.00704.x>
- 622 Cluzel, Dominique, Ulrich, M., Jourdan, F., Meffre, S., Paquette, J. L., Audet, M. A., et al. (2016). Early
 623 Eocene clinostatite boninite and boninite-series dikes of the ophiolite of New Caledonia; a witness of
 624 slab-derived enrichment of the mantle wedge in a nascent volcanic arc. *Lithos*, 260, 429–442.
 625 <https://doi.org/10.1016/j.lithos.2016.04.031>
- 626 Coogan, L. A., Jenkin, G. R. T., & Wilson, R. N. (2002). Constraining the cooling rate of the lower oceanic
 627 crust: A new approach applied to the Oman ophiolite. *Earth and Planetary Science Letters*, 199(1–2),
 628 127–146. [https://doi.org/10.1016/S0012-821X\(02\)00554-X](https://doi.org/10.1016/S0012-821X(02)00554-X)
- 629 Dimanov, A., & Wiedenbeck, M. (2006). (Fe,Mn)-Mg interdiffusion in natural diopside: effect of pO₂.
 630 *European Journal of Mineralogy*, 18(6), 705–718. <https://doi.org/10.1127/0935-1221/2006/0018-0705>
- 631 Dygert, N., & Liang, Y. (2015). Temperatures and cooling rates recorded in REE in coexisting pyroxenes in
 632 ophiolitic and abyssal peridotites. *Earth and Planetary Science Letters*, 420, 151–161.
 633 <https://doi.org/10.1016/j.epsl.2015.02.042>
- 634 Dygert, N., Liang, Y., & Kelemen, P. B. (2016). Formation of Plagioclase Lherzolite and Associated Dunite–
 635 Harzburgite–Lherzolite Sequences by Multiple Episodes of Melt Percolation and Melt–Rock Reaction:
 636 an Example from the Trinity Ophiolite, California, USA. *Journal of Petrology*, 57(4), 815–838.
 637 <https://doi.org/10.1093/petrology/egw018>
- 638 Dygert, N., Kelemen, P. B., & Liang, Y. (2017). Spatial variations in cooling rate in the mantle section of the
 639 Samail ophiolite in Oman: Implications for formation of lithosphere at mid-ocean ridges. *Earth and*
 640 *Planetary Science Letters*, 465, 134–144. <https://doi.org/10.1016/j.epsl.2017.02.038>
- 641 Faak, K., & Gillis, K. M. (2016). Slow cooling of the lowermost oceanic crust at the fast-spreading East
 642 Pacific Rise. *Geology*, 44(2), 115–118. <https://doi.org/10.1130/G37353.1>
- 643 Falloon, T. J., & Danyushevsky, L. V. (2000). Melting of Refractory Mantle at 1.5, 2 and 2.5 GPa under
 644 Anhydrous and H₂O-undersaturated Conditions: Implications for the Petrogenesis of High-Ca
 645 Boninites and the Influence of Subduction Components on Mantle Melting. *J. Petrol.*, 41(2), 257–283.
 646 <https://doi.org/10.1093/petrology/41.2.257>
- 647 Fumagalli, P., Borghini, G., Rampone, E., & Poli, S. (2017). Experimental calibration of Forsterite–
 648 Anorthite–Ca-Tschemak–Enstatite (FACE) geobarometer for mantle peridotites. *Contributions to*

- 649 *Mineralogy and Petrology*, 172(6), 38. <https://doi.org/10.1007/s00410-017-1352-2>
- 650 Ganguly, J., & Tirone, M. (1999). Diffusion closure temperature and age of a mineral with arbitrary extent of
651 diffusion: Theoretical formulation and applications. *Earth and Planetary Science Letters*, 170(1–2),
652 131–140. [https://doi.org/10.1016/S0012-821X\(99\)00089-8](https://doi.org/10.1016/S0012-821X(99)00089-8)
- 653 Garrido, C. J., Bodinier, J. L., Dhuime, B., Bosch, D., Chanefo, I., Bruguier, O., et al. (2007). Origin of the
654 island arc Moho transition zone via melt-rock reaction and its implications for intracrustal
655 differentiation of island arcs: Evidence from the Jijal complex (Kohistan complex, northern Pakistan).
656 *Geology*, 35(8), 683–686. <https://doi.org/10.1130/G23675A.1>
- 657 GREENE, A. R. (2006). A Detailed Geochemical Study of Island Arc Crust: the Talkeetna Arc Section,
658 South-Central Alaska. *Journal of Petrology*, 47(6), 1051–1093.
659 <https://doi.org/10.1093/petrology/egl002>
- 660 Guo, P., Xu, W. L., Wang, C. G., & Zhang, Y. L. (2019). Thermal state and structure of lithospheric mantle
661 beneath the Xing'an Massif, northeast China: Constraints from mantle xenoliths entrained by Cenozoic
662 basalts. *Geological Journal*, 54(6), 3226–3238. <https://doi.org/10.1002/gj.3322>
- 663 Hanghøj, K., Kelemen, P.B., Hassler, D., Godard, M. (2010). Composition and Genesis of Depleted Mantle
664 Peridotites from the Wadi Tayin Massif, Oman Ophiolite; Major and Trace Element Geochemistry, and
665 Os Isotope and PGE Systematics. *Journal of Petrology*, 51, 201–227.
- 666 De Hoog, J.C.M., Gall, L., and Cornell, D. H. (2010). Trace-element geochemistry of mantle olivine and
667 application to mantle petrogenesis and geothermobarometry. *Chemical Geology*, 270, 196–215.
- 668 Jean, M. M., Shervais, J. W., Choi, S.-H., & Mukasa, S. B. (2010). Melt extraction and melt refertilization in
669 mantle peridotite of the Coast Range ophiolite: an LA–ICP–MS study. *Contributions to Mineralogy
670 and Petrology*, 159(1), 113–136. <https://doi.org/10.1007/s00410-009-0419-0>
- 671 Jianping, L., Kornprobst, J., Vielzeuf, D., & Fabriès, J. (1995). An improved experimental calibration of the
672 olivine-spinel geothermometer. *Chinese Journal of Geochemistry*, 14(1), 68–77.
673 <https://doi.org/10.1007/BF02840385>
- 674 Johnson, K. T. M., Dick, H. J. B., & Shimizu, N. (1990). Melting in the Oceanic Upper Mantle: An Ion
675 Microprobe Study of Diopsides in Abyssal Peridotites. *Journal of Geophysical Research*, 95(B3), 2661.
676 <https://doi.org/10.1029/JB095iB03p02661>
- 677 Khedr, M. Z., Arai, S., Python, M., & Tamura, A. (2014). Chemical variations of abyssal peridotites in the
678 central Oman ophiolite: Evidence of oceanic mantle heterogeneity. *Gondwana Research*, 25(3), 1242–
679 1262. <https://doi.org/10.1016/j.gr.2013.05.010>
- 680 Lagabriele, Y., Chauvet, A., Ulrich, M., & Guillot, S. (2013). Passive obduction and gravity-driven
681 emplacement of large ophiolitic sheets: The New Caledonia ophiolite (SW Pacific) as a case study?
682 *Bulletin de La Societe Geologique de France*, 184(6), 545–556.
683 <https://doi.org/10.2113/gssgfbull.184.6.545>
- 684 Lee, Cin Ty A., & Chin, E. J. (2014). Calculating melting temperatures and pressures of peridotite protoliths:
685 Implications for the origin of cratonic mantle. *Earth and Planetary Science Letters*, 403, 273–286.

- 686 <https://doi.org/10.1016/j.epsl.2014.06.048>
- 687 Lee, Cin Ty Aeolus, Harbert, A., & Leeman, W. P. (2007). Extension of lattice strain theory to
688 mineral/mineral rare-earth element partitioning: An approach for assessing disequilibrium and
689 developing internally consistent partition coefficients between olivine, orthopyroxene, clinopyroxene
690 and basaltic melt. *Geochimica et Cosmochimica Acta*, 71(2), 481–496.
691 <https://doi.org/10.1016/j.gca.2006.09.014>
- 692 Liang, Y., Sun, C., & Yao, L. (2013a). A REE-in-two-pyroxene thermometer for mafic and ultramafic rocks.
693 *Geochimica et Cosmochimica Acta*, 102, 246–260. <https://doi.org/10.1016/j.gca.2012.10.035>
- 694 Liang, Y., Sun, C., & Yao, L. (2013b). A REE-in-two-pyroxene thermometer for mafic and ultramafic rocks.
695 *Geochimica et Cosmochimica Acta*, 102, 246–260. <https://doi.org/10.1016/j.gca.2012.10.035>
- 696 Lindsley, D. H. (1983). Pyroxene thermometry. *American Mineralogist*, 68(5–6), 477–493. Retrieved from
697 [https://pubs.geoscienceworld.org/msa/ammin/article-abstract/68/5-6/477/104808/pyroxene-](https://pubs.geoscienceworld.org/msa/ammin/article-abstract/68/5-6/477/104808/pyroxene-thermometry)
698 thermometry
- 699 Marchesi, C., Jolly, W. T., Lewis, J. F., Garrido, C. J., Proenza, J. A., & Lidiak, E. G. (2011). Petrogenesis of
700 fertile mantle peridotites from the Monte del Estado massif (Southwest Puerto Rico): A preserved
701 section of Proto-Caribbean lithospheric mantle? *Geologica Acta*, 9(3), 289–306.
702 <https://doi.org/10.1344/105.000001713>
- 703 Marchesi, Claudio, Garrido, C. J., Godard, M., Belley, F., & Ferré, E. (2009). Migration and accumulation of
704 ultra-depleted subduction-related melts in the Massif du Sud ophiolite (New Caledonia). *Chemical*
705 *Geology*, 266(3–4), 171–186. <https://doi.org/10.1016/j.chemgeo.2009.06.004>
- 706 McGoldrick, S., Canil, D., & Zagorevski, A. (2018). Contrasting thermal and melting histories for segments
707 of mantle lithosphere in the Nahlin ophiolite, British Columbia, Canada. *Contributions to Mineralogy*
708 *and Petrology*, 173(3), 1–17. <https://doi.org/10.1007/s00410-018-1450-9>
- 709 Muntener, O., Manatschal, G., Desmurs, L., & Pettke, T. (2010). Plagioclase Peridotites in Ocean-Continent
710 Transitions: Refertilized Mantle Domains Generated by Melt Stagnation in the Shallow Mantle
711 Lithosphere. *Journal of Petrology*, 51(1–2), 255–294. <https://doi.org/10.1093/petrology/egp087>
- 712 Ohara, Y., & Ishii, T. (1998). Peridotites from the southern Mariana forearc: Heterogeneous fluid supply in
713 mantle wedge. *Island Arc*, 7(3), 541–558. <https://doi.org/10.1111/j.1440-1738.1998.00209.x>
- 714 Parkinson, I. J., & Pearce, J. a. (1998). Peridotites from the Izu-Bonin-Mariana forearc (ODP leg 125):
715 Evidence for mantle melting and melt-mantle interaction in a supra-subduction zone setting. *Journal of*
716 *Petrology*, 39(9), 1577–1618. <https://doi.org/10.1093/etroj/39.9.1577>
- 717 Pirard, C., Hermann, J., & O'Neill, H. S. C. (2013). Petrology and Geochemistry of the Crust-Mantle
718 Boundary in a Nascent Arc, Massif du Sud Ophiolite, New Caledonia, SW Pacific. *Journal of*
719 *Petrology*, 54(9), 1759–1792. <https://doi.org/10.1093/petrology/egt030>
- 720 Prinzhofer, A. et Allègre, C. (1985). Residual peridotites and the mechanisms of partial melting. *Earth*
721 *Planetary Science Letters*, 74(2–3), 251–265.
- 722 Prinzhofer, A., & Nicolas, A. (2015). The Bogota Peninsula, New Caledonia: A Possible Oceanic Transform

- 723 Fault. <https://doi.org/10.1086/628523>, 88(4), 387–398. <https://doi.org/10.1086/628523>
- 724 Putirka, K. D. (2008). Thermometers and barometers for volcanic systems. *Reviews in Mineralogy and*
725 *Geochemistry*, 69(1), 61–120. <https://doi.org/10.2138/rmg.2008.69.3>
- 726 Riches, A. J. V., & Rogers, N. W. (2011). Mineralogical and geochemical constraints on the shallow origin,
727 ancient veining, and multi-stage modification of the Lherz peridotite. *Geochimica et Cosmochimica*
728 *Acta*, 75(20), 6160–6182. <https://doi.org/10.1016/j.gca.2011.07.036>
- 729 Schellart, W. P., Lister, G. S., & Toy, V. G. (2006). A Late Cretaceous and Cenozoic reconstruction of the
730 Southwest Pacific region: Tectonics controlled by subduction and slab rollback processes. *Earth-*
731 *Science Reviews*, 76(3–4), 191–233. <https://doi.org/10.1016/j.earscirev.2006.01.002>
- 732 Secchiari, A., Montanini, A., Bosch, D., Macera, P., & Cluzel, D. (2016). Lithos Melt extraction and
733 enrichment processes in the New Caledonia lherzolites : Evidence from geochemical and Sr – Nd
734 isotope data. *LITHOS*, 260, 28–43. <https://doi.org/10.1016/j.lithos.2016.04.030>
- 735 Secchiari, A., Montanini, A., Bosch, D., Macera, P., & Cluzel, D. (2018). The contrasting geochemical
736 message from the New Caledonia gabbro-norites: insights on depletion and contamination processes of
737 the sub-arc mantle in a nascent arc setting. *Contributions to Mineralogy and Petrology*, 173(8), 66.
738 <https://doi.org/10.1007/s00410-018-1496-8>
- 739 Secchiari, A., Montanini, A., Bosch, D., Macera, P., & Cluzel, D. (2019). Origin of the spinel-pyroxene
740 symplectites in the harzburgites from the New Caledonia peridotite. *Ophioliti*, 44(1), 31–42.
741 <https://doi.org/10.4454/ofioliti.v44i1.463>
- 742 Secchiari, A., Montanini, A., Bosch, D., Macera, P., & Cluzel, D. (2020). Sr, Nd, Pb and trace element
743 systematics of the New Caledonia harzburgites: Tracking source depletion and contamination processes
744 in a SSZ setting. *Geoscience Frontiers*, 11(1), 37–55. <https://doi.org/10.1016/j.gsf.2019.04.004>
- 745 Smye, A., Seaman, S., Hudak, M., & Crispin, K. (2017). Rates of mantle cooling and exhumation during
746 rifting constrained by REE-in-pyroxene speedometry. *Geochemistry, Geophysics, Geosystems*, 18,
747 1580–1593. <https://doi.org/10.1002/2017GC006821>
- 748 Sun, C., & Liang, Y. (2014). An assessment of subsolidus re-equilibration on REE distribution among
749 mantle minerals olivine, orthopyroxene, clinopyroxene, and garnet in peridotites. *Chemical Geology*,
750 372, 80–91. <https://doi.org/10.1016/J.CHEMGEO.2014.02.014>
- 751 Sun, C., & Liang, Y. (2017a). A REE-in-plagioclase–clinopyroxene thermometer for crustal rocks.
752 *Contributions to Mineralogy and Petrology*, 172(4), 24. <https://doi.org/10.1007/s00410-016-1326-9>
- 753 Sun, C., & Liang, Y. (2017b). A REE-in-plagioclase–clinopyroxene thermometer for crustal rocks.
754 *Contributions to Mineralogy and Petrology*, 172(4), 1–20. <https://doi.org/10.1007/s00410-016-1326-9>
- 755 Takazawa, E., Okayasu, T., & Satoh, K. (2003). Geochemistry and origin of the basal lherzolites from the
756 northern Oman ophiolite (northern Fizh block). *Geochemistry, Geophysics, Geosystems*, 4(2), n/a-n/a.
757 <https://doi.org/10.1029/2001GC000232>
- 758 Taylor, & R., W. (1998). An experimental test of some geothermometer and geobarometer formulations for
759 upper mantle peridotites with application to the thermobarometry of fertile lherzolite and

- 760 garnetwebsterite. *Neues Jahrbuch Für Mineralogie - Abhandlungen*, 381–408.
 761 <https://doi.org/10.1127/NJMA/172/1998/381>
- 762 Titus, S. J., Maes, S. M., Benford, B., Ferré, E. C., & Tikoff, B. (2011). Fabric development in the mantle
 763 section of a paleotransform fault and its effect on ophiolite obduction, New Caledonia. *Lithosphere*,
 764 3(3), 221–244. <https://doi.org/10.1130/L122.1>
- 765 Warren, J. M., Shimizu, N., Sakaguchi, C., Dick, H. J. B., & Nakamura, E. (2009). An assessment of upper
 766 mantle heterogeneity based on abyssal peridotite isotopic compositions. *Journal of Geophysical*
 767 *Research*, 114(B12), B12203. <https://doi.org/10.1029/2008JB006186>
- 768 Warren, Jessica M. (2016, April 1). Global variations in abyssal peridotite compositions. *Lithos*. Elsevier.
 769 <https://doi.org/10.1016/j.lithos.2015.12.023>
- 770 Wells, P. R. A. (1977). Pyroxene thermometry in simple and complex systems. *Contributions to Mineralogy*
 771 *and Petrology*, 62(2), 129–139. <https://doi.org/10.1007/BF00372872>
- 772 Whattam, S. a. (2009). Arc-continent collisional orogenesis in the SW Pacific and the nature, source and
 773 correlation of emplaced ophiolitic nappe components. *Lithos*, 113(1–2), 88–114.
 774 <https://doi.org/10.1016/j.lithos.2008.11.009>
- 775 Xu, Y., Liu, C. zhou, & Lin, W. (2020). Melt extraction and reaction in the forearc mantle: Constraints from
 776 trace elements and isotope geochemistry of ultra-refractory peridotites of the New Caledonia Peridotite
 777 Nappe. *Lithos*, 105882. <https://doi.org/10.1016/j.lithos.2020.105882>
- 778 Zanetti, A., D'Antonio, M., Spadea, P., Raffone, N., Vannucci, R., & Brugier, O. (2006). Petrogenesis of
 779 mantle peridotites from the Izu-Bonin-Mariana (IBM) Forearc. *Ophioliti*, 31(2), 189–206.

780
 781

782 Figure captions

783

784 Figure 1. a) Present-day structures of the Southwest Pacific region. Dark orange, land; light orange, continental
 785 plateau; white, oceanic basins (LHR: Lord Howe Rise, NR: Norfolk ridge, LR: Loyalty ridge, HP: Hikurangi
 786 Plateau); b) simplified geological map of New Caledonia showing the distribution of the Peridotite massifs
 787 and sampling locations (i.e. red stars); c) simplified sketch map of the southern part of the Massif du Sud. Red
 788 stars: sampling areas for the gabbro-norites (Secchiari et al., 2018, see Table 1). Black and blue stars are
 789 sampling locations of the mafic-ultramafic sequence and the harzburgites from the work of Marchesi et al.
 790 (2009) and Pirard et al. (2013), respectively. Modified after Cluzel et al. (2012) and Secchiari et al. (2018).

791

792 Figure 2. Chondrite-normalized REE compositions of a) clino- and orthopyroxene from the New Caledonia
 793 spinel lherzolites and b) plagioclase lherzolites (Secchiari et al., 2016); c) clinopyroxene and d) plagioclase
 794 from the New Caledonia gabbro-norites (Secchiari et al., 2018).

795 Plotted values represent average values for each sample. Error bars are smaller or equal to the symbol size.

796

797 Figure 3. a) Orthopyroxene/clinopyroxene REE partition coefficients calculated for the New Caledonia
798 lherzolites and gabbroonorites. The lherzolites follow the opx/cpx partitioning trends predicted for temperatures
799 of 1300-1400 °C, while the gabbroonorites depict scattered trends, indicative of pyroxenes disequilibrium.
800 Opx/cpx partitioning trends at 1000 °C, 1300 °C and 1400 °C are from Lee et al. (2007). Light blue area =
801 abyssal peridotites field. b-c) Pl/Cpx REE-Y ratios plotted against their ionic radius for PL1 and PR3
802 gabbroonorites, respectively. Equilibration temperature lines were calculated based on mineral major element
803 compositions compositions using the Pl/Cpx partitioning model of Sun and Liang (2012) and Sun et al. (2017).
804

805 Figure 4. Comparison of temperatures derived from the REE-in-two-pyroxene thermometer ($T_{\text{REE-Y}}$, Liang et
806 al., 2013) with temperatures from a) two-pyroxene thermometer (T_{BKN} , Brey and Köhler, 1990); b) Ca-in-
807 orthopyroxene thermometer ($T_{\text{Ca-in-Opx}}$, Brey and Köhler, 1990) and c) olivine-spinel thermometer ($T_{\text{Ol-Spl}}$, Li
808 et al., 1995). 4d): diagram showing closure temperature cooling curves (red lines) calculated for initial peak
809 temperatures on the solidus (T_0) followed by cooling at various rates (in °C/year - vertical black lines) to the
810 final closure temperatures of T_{REE} and T_{BKN} for an average 2.5 mm grain radius of orthopyroxene. The
811 calculations follow the method and diffusion parameters for REE and Fe-Mg diffusion in pyroxenes outlined
812 in Dygert et al. (2017). Pink and light grey fields represent abyssal and ophiolitic peridotites, respectively,
813 from Dygert et al. (2017). Light yellow field: supra-subduction zone peridotites (Canil et al., 2019).

814
815 Figure 5. Results of $T_{\text{Ca-in-Ol}}$ (De Hoog et al., 2006) plotted against $T_{\text{Ol-Sp}}$ (Li et al., 1995). Field of abyssal
816 peridotites includes data from Warren (2016). Data sources for ophiolites: Aldanmaz, (2012) ; Barth et al.
817 (2003); Batanova et al. (2011); Dygert and Liang (2015); Dygert et al. (2016) ; Jean et al. (2010) ; Khedr et al.
818 (2014); Marchesi et al. (2011); Muntener et al. (2010) ; Riches and Rogers (2011); Takazawa et al. (2003).

819
820 Figure 6. a) Simplified schematic representation of the stratigraphy in the Massif du Sud sequence; b)
821 temperature profiles and c) olivine cooling rates extending from the lower crust to the depleted mantle.
822 Temperatures profiles were built using average temperature values for each geothermometer. Olivine cooling
823 rates are reported as average cooling rates for each lithology (i.e. gabbroonorites, wehrlites and harzburgites).

824

Figure 1.

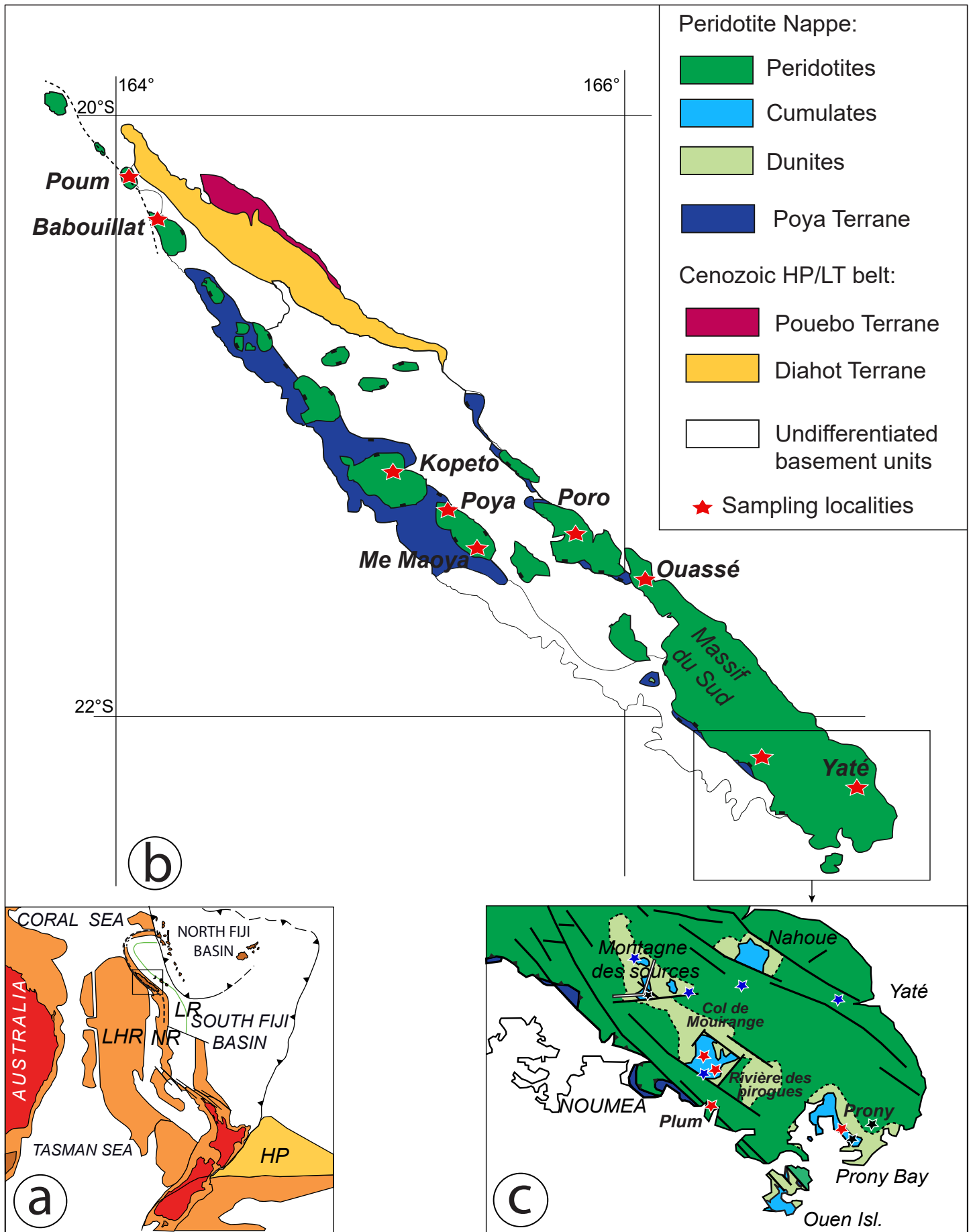


Figure 2.

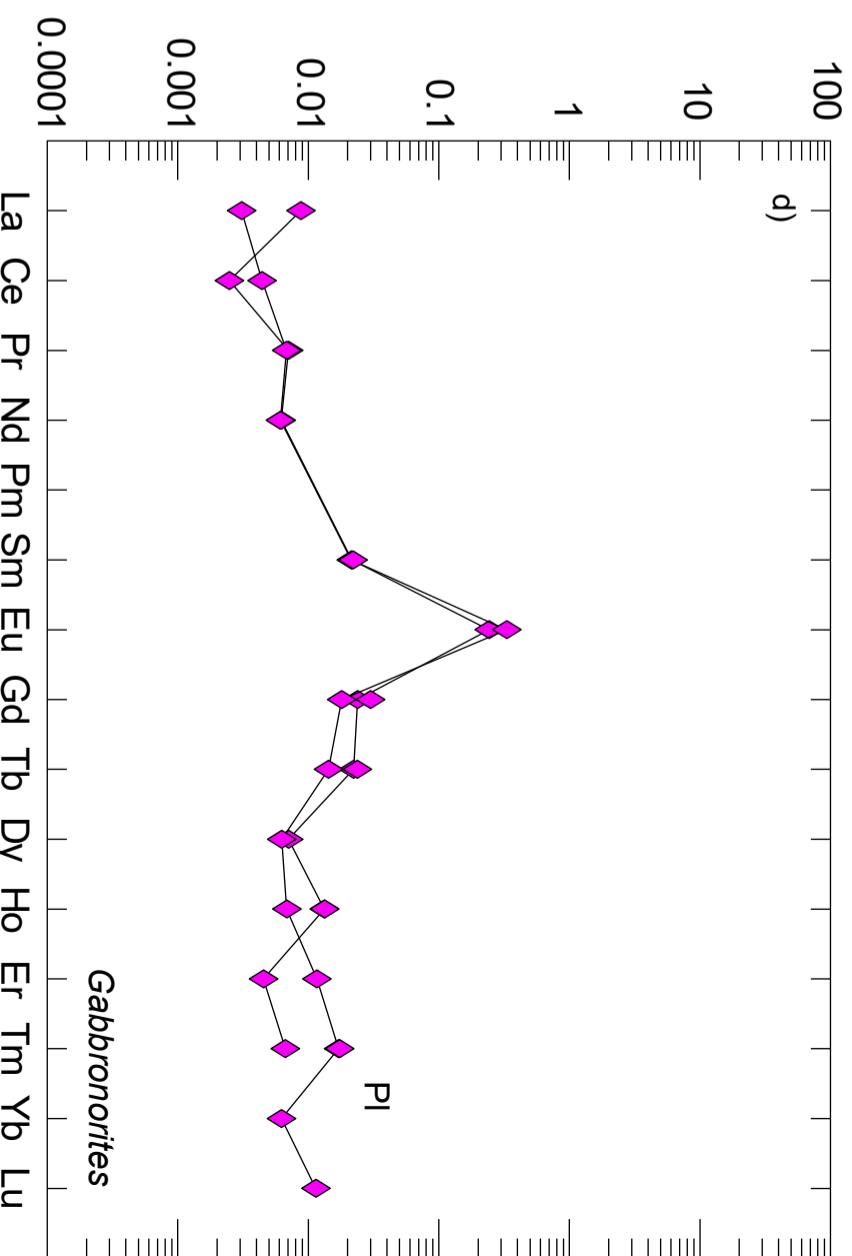
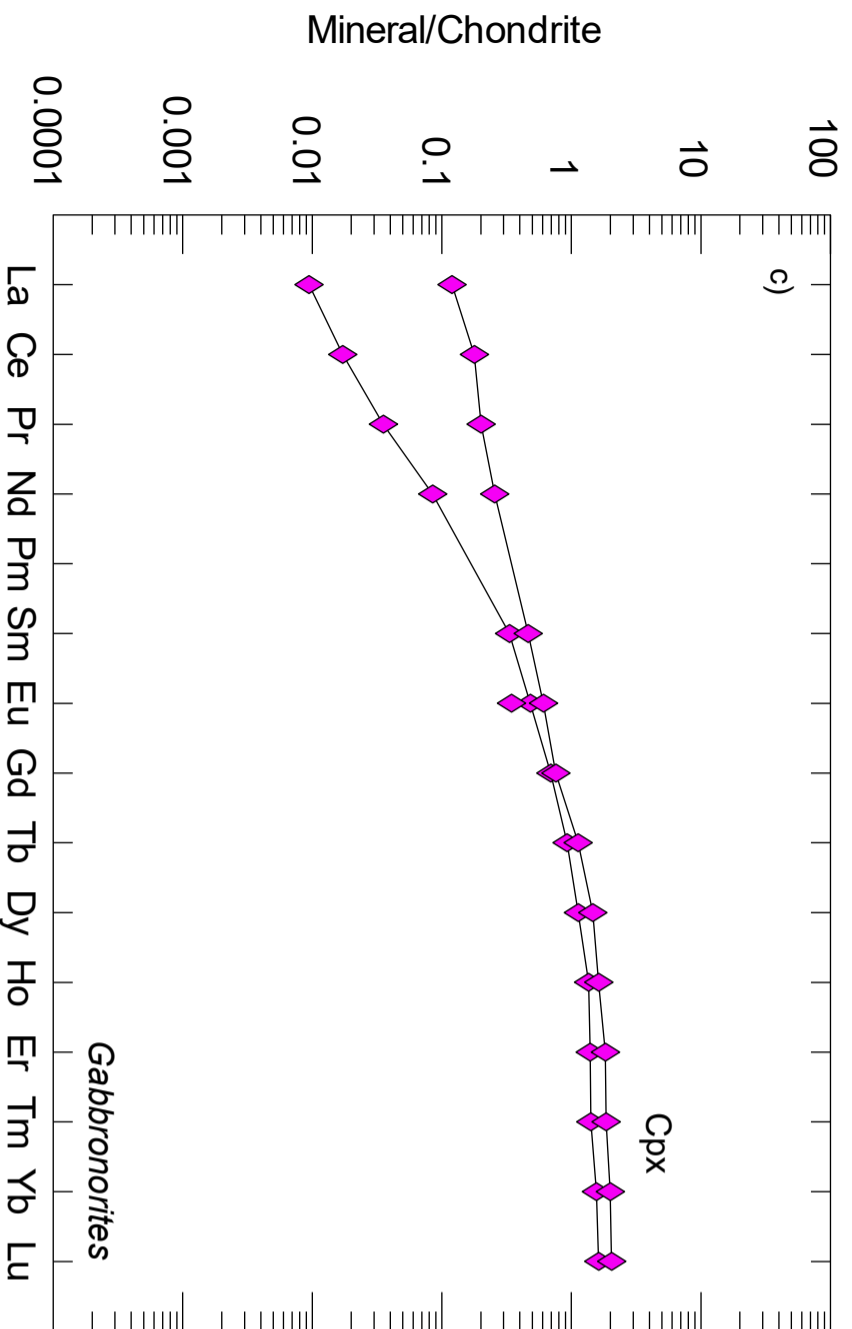
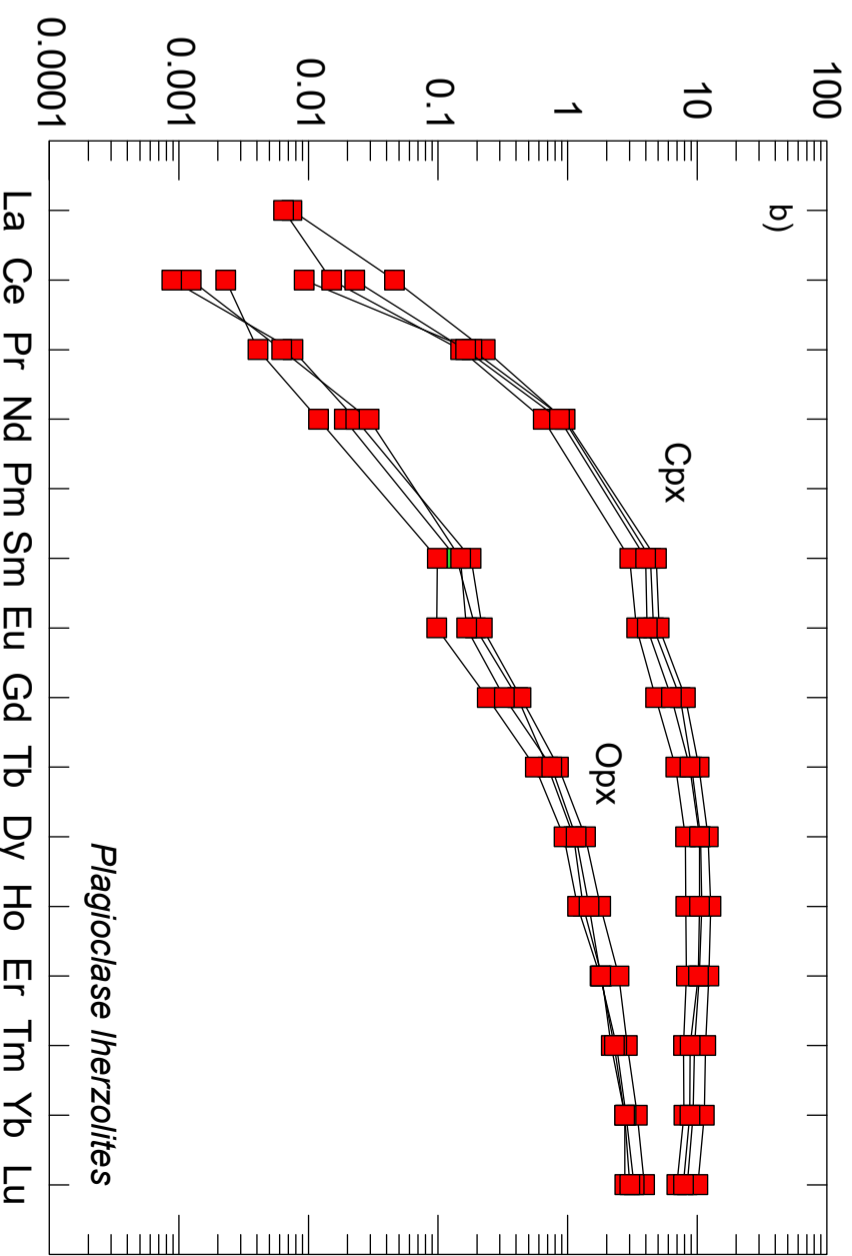
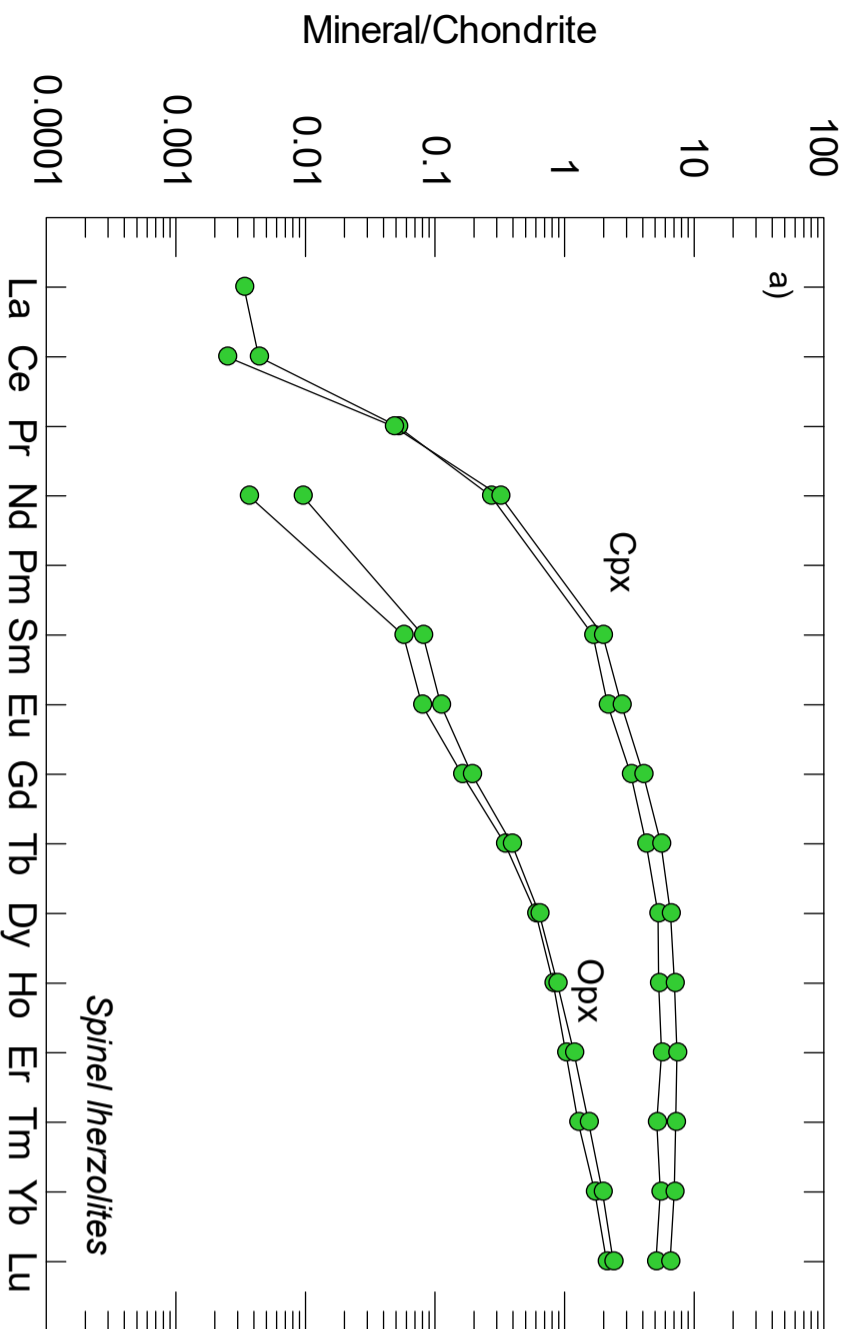


Figure 3.

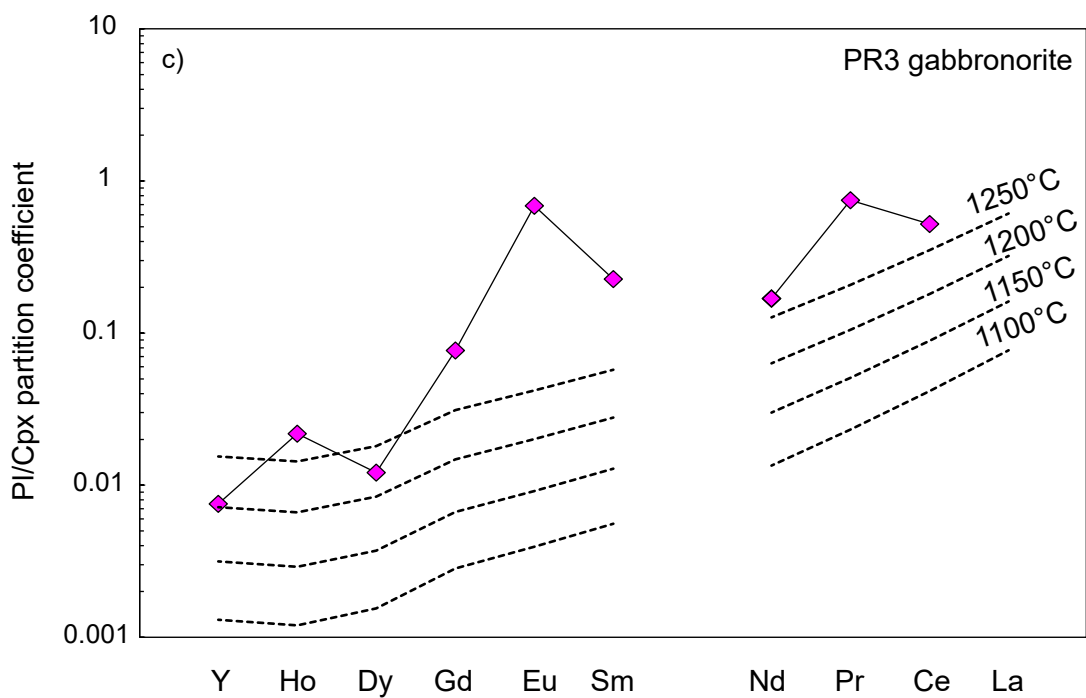
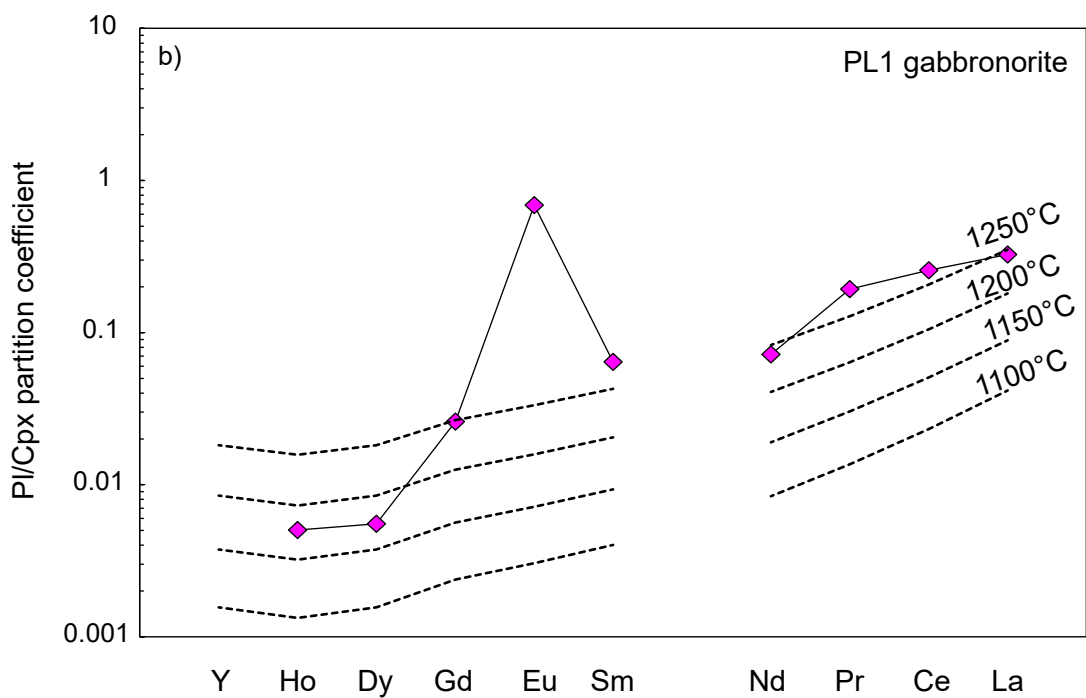
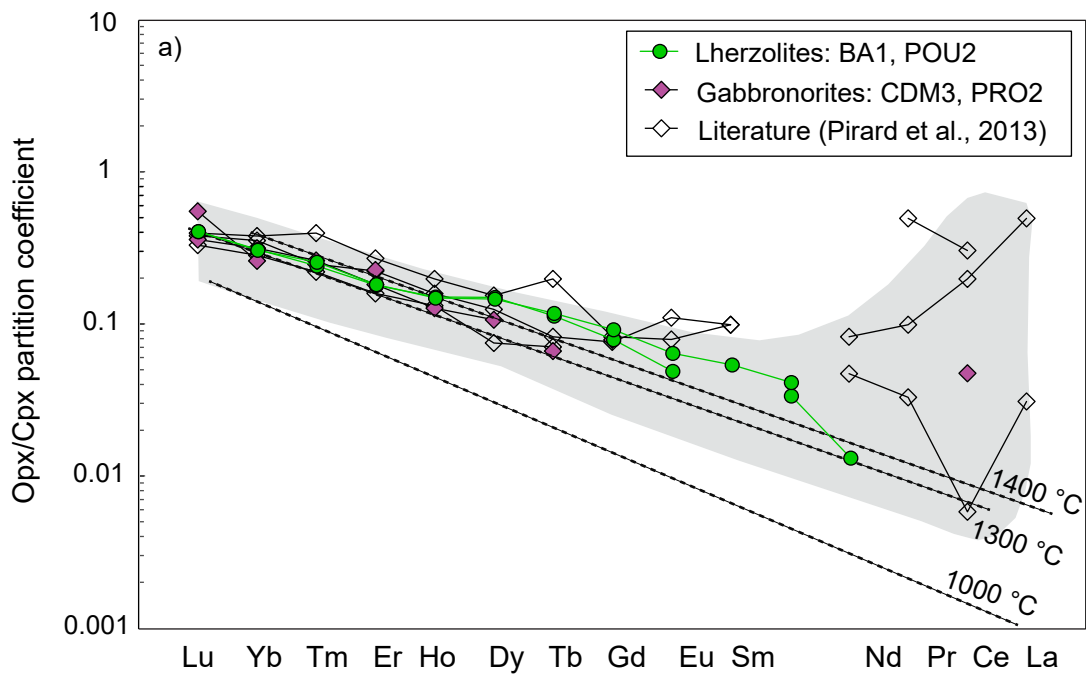


Figure 4.

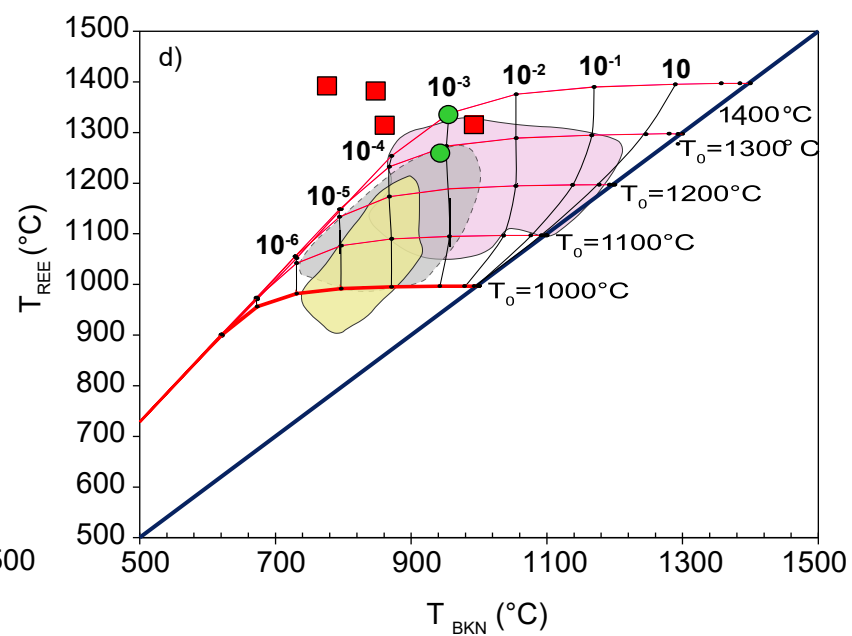
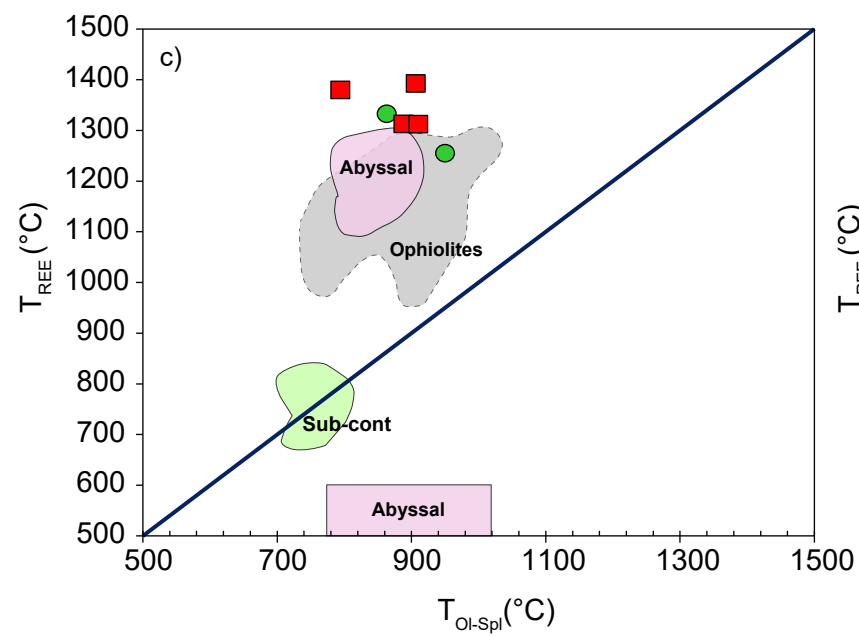
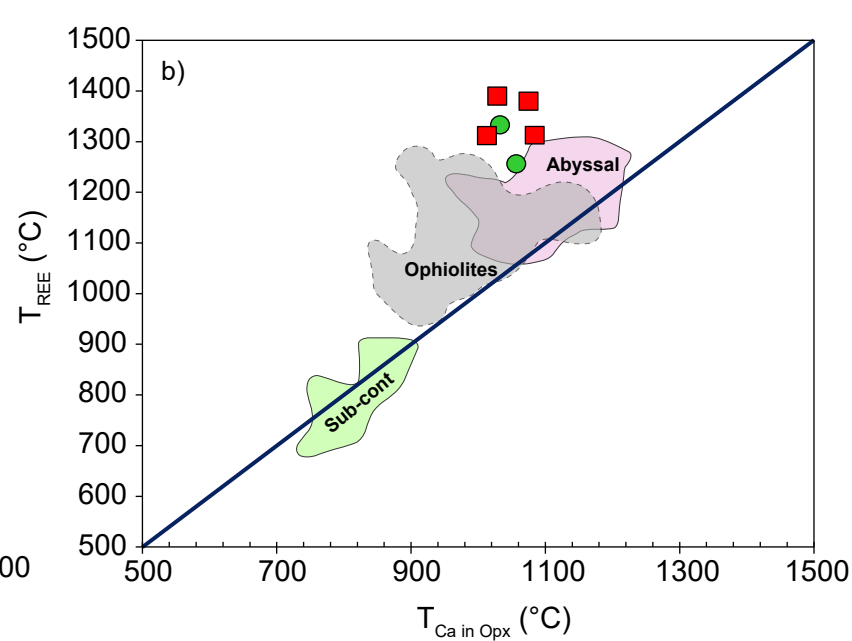
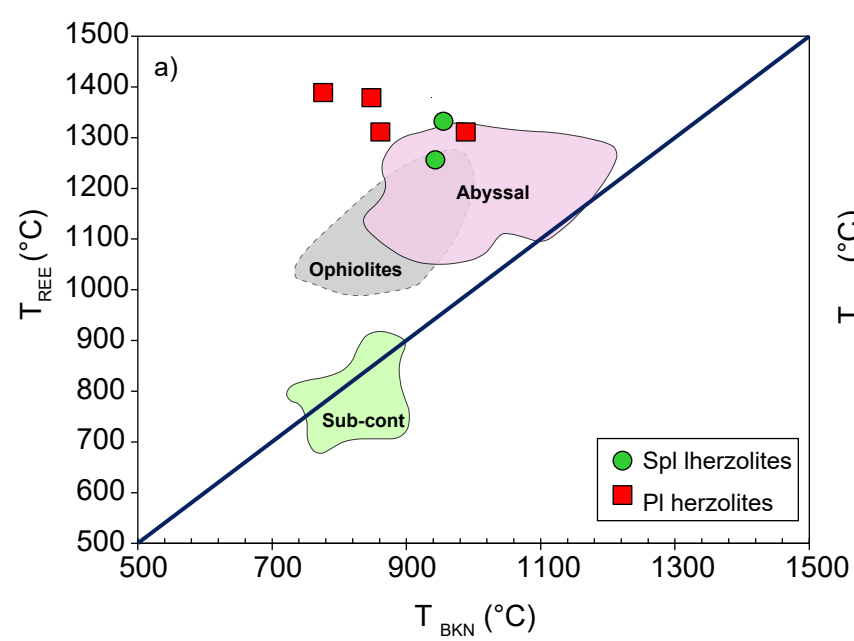


Figure 5.

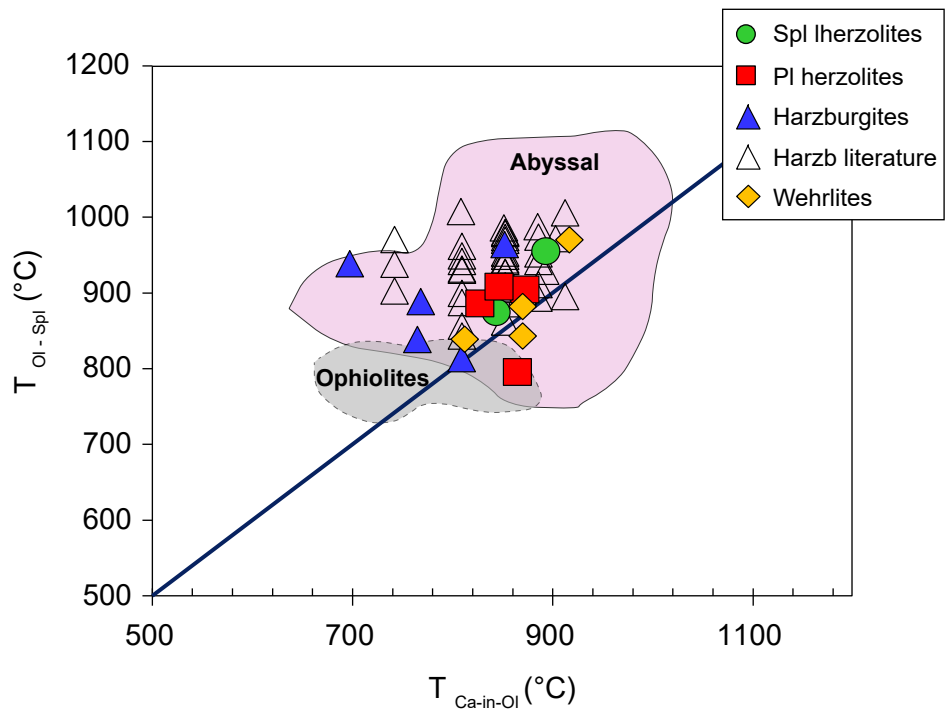


Figure 6.

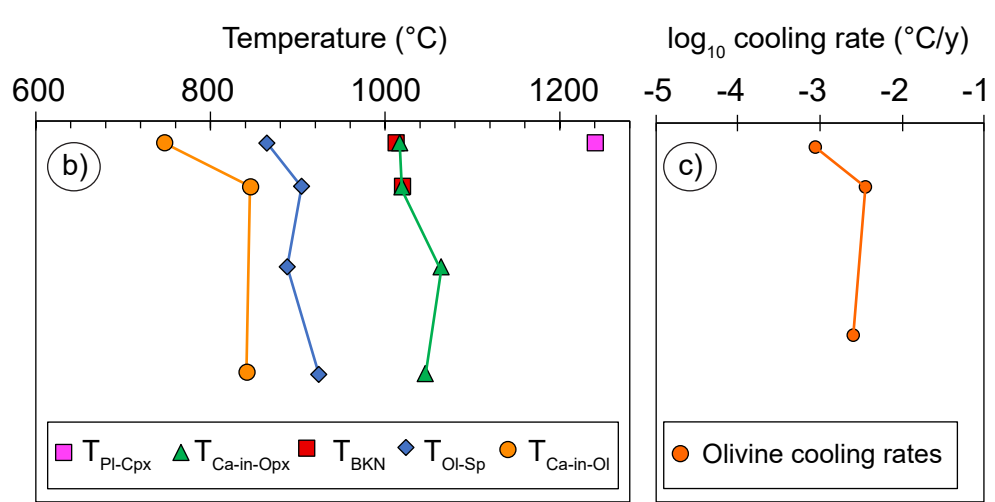
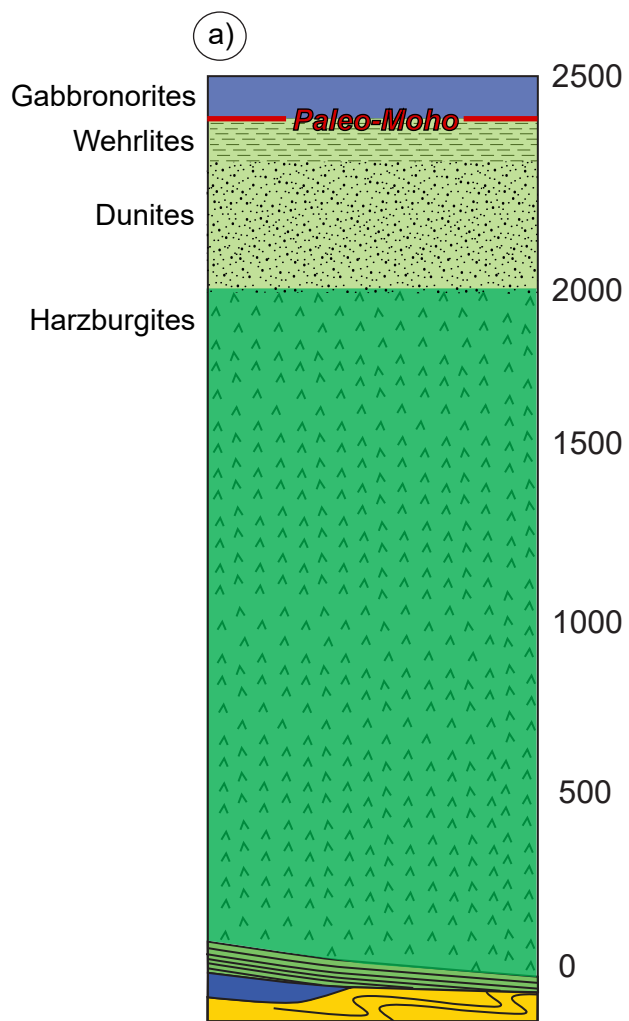


Table 1. Equilibrium temperatures and cooling rates calculated for the New Caledonia peridotites.

Sample	Locality	Lithology	Source	T_{REE-Y}	$\pm 1\sigma$	T_{BKN}	T_{Ta}	$T_{Ca-in-Opx}$	$T_{Ca-in-Ol}$	T_{Ol-Sp}	Opx radius (mm)	dT/dt (°C/y) from T_{REE-Y} and T_{BKN}	Ol radius (mm) [‡]	dT/dt (°C/y) from $T_{Ca-in-Ol}$
BA1	Babouillat	Spl lherzolite	Secchiari et al. (2016)	1334	39	955	960	1031	824	863	2.5	4.00E-03	1.0	1.17E-03
BAB1B	Babouillat	Pl lherzolite	Secchiari et al. (2016)	1314	24	993	1026	1082	828	888	2.5	4.00E-03	1.0	1.27E-03
BAB2A	Babouillat	Pl lherzolite	Secchiari et al. (2016)	1381	7	847	844	1074	865	794	-	-	1.0	2.85E-03
BAB2B	Babouillat	Pl lherzolite	Secchiari et al. (2016)	1394	25	776	758	1027	873	906	-	-	1.0	3.34E-03
POU2	Poum	Spl lherzolite	Secchiari et al. (2016)	1256	11	946	967	1055	893	950	2.5	4.00E-03	1.0	5.10E-03
POU1A	Poum	Pl lherzolite	Secchiari et al. (2016)	1311	33	861	876	1010	847	910	-	-	1.0	1.93E-03
KPT1*	Kopeto	Harzburgite	Secchiari et al. (2020)	-	-	-	-	1125	853	965	-	-	0.8	3.43E-03
KPT3*	Kopeto	Harzburgite	Secchiari et al. (2020)	-	-	-	-	1024	769	890	-	-	0.8	4.99E-04
KPT5*	Kopeto	Spl harzburgite	Secchiari et al. (2020)	-	-	-	-	1030	766	840	-	-	0.8	4.58E-04
PY1*	Poya	Spl harzburgite	Secchiari et al. (2020)	-	-	e	-	1017	-	930	-	-	-	-
PO3*	Poro	Spl harzburgite	Secchiari et al. (2020)	-	-	-	-	986	-	940	-	-	-	-
PO4*	Poro	Spl harzburgite	Secchiari et al. (2020)	-	-	-	-	-	811	-	-	-	0.8	1.35E-03
YA1*	Yaté	Spl harzburgite	Secchiari et al. (2020)	-	-	-	-	1020	810	815	-	-	1.0	8.44E-04
MM1*	Me Maoya	Spl harzburgite	Secchiari et al., unpubl.	-	-	-	-	976	-	910	-	-	-	-
MM2*	Me Maoya	Spl harzburgite	Secchiari et al., unpubl.	-	-	-	-	1011	-	900	-	-	-	-
TT4A*	Tontouta valley	Harzburgite	Marchesi et al. (2009)	-	-	-	-	991	884	933	-	-	1.0	4.26E-03
TT14*	Tontouta valley	Harzburgite	Marchesi et al. (2009)	-	-	-	-	1095	851	954	-	-	1.0	2.14E-03
TT17*	Tontouta valley	Harzburgite	Marchesi et al. (2009)	-	-	-	-	1070	851	-	-	-	1.0	2.14E-03
PR 4B*	Prony	Harzburgite	Marchesi et al. (2009)	-	-	-	-	1008	808	-	-	-	1.0	8.12E-04
PR 5B*	Prony	Harzburgite	Marchesi et al. (2009)	-	-	-	-	986	851	-	-	-	1.0	2.12E-03
YA5*	Yaté	Harzburgite	Pirard et al. (2013)	-	-	-	-	929	892	-	-	-	1.0	4.98E-03
PRB5b*	Parc de la Rivière Bleue	Harzburgite	Pirard et al. (2013)	-	-	-	-	1106	938	931	-	-	1.0	1.20E-02
PRB61f*	Parc de la Rivière Bleue	Harzburgite	Pirard et al. (2013)	-	-	-	-	-	894	875	-	-	1.0	5.18E-03
PRB75*	Parc de la Rivière Bleue	Harzburgite	Pirard et al. (2013)	-	-	-	-	972	902	910	-	-	1.0	6.10E-03
15NC01*	Ouassé Bay	Harzburgite	Xu et al. (2020)	-	-	-	-	1067	851	907	-	-	1.0	2.14E-03
15NC02*	Ouassé Bay	Harzburgite	Xu et al. (2020)	-	-	-	-	916	808	858	-	-	1.0	8.12E-04
15NC03*	Ouassé Bay	Harzburgite	Xu et al. (2020)	-	-	-	-	1116	851	974	-	-	1.0	2.14E-03
15NC04*	Ouassé Bay	Harzburgite	Xu et al. (2020)	-	-	-	-	1145	808	844	-	-	1.0	8.12E-04
15NC05*	Ouassé Bay	Harzburgite	Xu et al. (2020)	-	-	-	-	1000	851	942	-	-	1.0	2.14E-03
15NC06*	Ouassé Bay	Harzburgite	Xu et al. (2020)	-	-	-	-	903	851	981	-	-	1.0	2.14E-03
15NC07*	Ouassé Bay	Harzburgite	Xu et al. (2020)	-	-	-	-	1037	808	950	-	-	1.0	8.12E-04
15NC08*	Ouassé Bay	Harzburgite	Xu et al. (2020)	-	-	-	-	1089	884	953	-	-	1.0	4.26E-03
15NC09*	Ouassé Bay	Harzburgite	Xu et al. (2020)	-	-	-	-	923	851	954	-	-	1.0	2.14E-03
15NC11*	Me Maoya	Harzburgite	Xu et al. (2020)	-	-	-	-	996	851	887	-	-	1.0	2.14E-03
15NC12*	Me Maoya	Harzburgite	Xu et al. (2020)	-	-	-	-	1100	808	888	-	-	1.0	8.12E-04
15NC13*	Me Maoya	Harzburgite	Xu et al. (2020)	-	-	-	-	985	851	980	-	-	1.0	2.14E-03
15NC15*	Me Maoya	Harzburgite	Xu et al. (2020)	-	-	-	-	1003	851	949	-	-	1.0	2.14E-03
15NC17*	Me Maoya	Harzburgite	Xu et al. (2020)	-	-	-	-	1039	884	912	-	-	1.0	4.26E-03
15NC20*	Me Maoya	Harzburgite	Xu et al. (2020)	-	-	-	-	1116	851	928	-	-	1.0	2.14E-03
15NC21*	Me Maoya	Harzburgite	Xu et al. (2020)	-	-	-	-	1025	808	931	-	-	1.0	8.12E-04
15NC22*	Me Maoya	Harzburgite	Xu et al. (2020)	-	-	-	-	1065	884	943	-	-	1.0	4.26E-03
15NC23*	Me Maoya	Harzburgite	Xu et al. (2020)	-	-	-	-	935	808	933	-	-	1.0	8.12E-04
15NC24*	Me Maoya	Harzburgite	Xu et al. (2020)	-	-	-	-	1006	851	945	-	-	1.0	2.14E-03
15NC25*	Me Maoya	Harzburgite	Xu et al. (2020)	-	-	-	-	1030	808	942	-	-	1.0	8.12E-04
15NC26*	Me Maoya	Harzburgite	Xu et al. (2020)	-	-	-	-	1102	911	896	-	-	1.0	7.29E-03
15NC27*	Me Maoya	Harzburgite	Xu et al. (2020)	-	-	-	-	917	741	904	-	-	1.0	1.56E-04
15NC28*	Me Maoya	Harzburgite	Xu et al. (2020)	-	-	-	-	1120	884	975	-	-	1.0	4.26E-03
15NC29*	Me Maoya	Harzburgite	Xu et al. (2020)	-	-	-	-	977	851	906	-	-	1.0	2.14E-03
15NC30*	Me Maoya	Harzburgite	Xu et al. (2020)	-	-	-	-	942	884	894	-	-	1.0	4.26E-03
15NC31*	Massif du Sud	Harzburgite	Xu et al. (2020)	-	-	-	-	992	851	963	-	-	1.0	2.14E-03
15NC32*	Massif du Sud	Harzburgite	Xu et al. (2020)	-	-	-	-	1028	808	901	-	-	1.0	8.12E-04
15NC33*	Massif du Sud	Harzburgite	Xu et al. (2020)	-	-	-	-	1075	851	928	-	-	1.0	2.14E-03
15NC34*	Massif du Sud	Harzburgite	Xu et al. (2020)	-	-	-	-	1185	741	939	-	-	1.0	1.56E-04
15NC84*	Massif du Sud	Harzburgite	Xu et al. (2020)	-	-	-	-	981	741	971	-	-	1.0	1.56E-04
15NC85*	Massif du Sud	Harzburgite	Xu et al. (2020)	-	-	-	-	941	911	1007	-	-	1.0	7.29E-03
15NC86*	Massif du Sud	Harzburgite	Xu et al. (2020)	-	-	-	-	978	808	963	-	-	1.0	8.12E-04
15NC87*	Massif du Sud	Harzburgite	Xu et al. (2020)	-	-	-	-	954	851	970	-	-	1.0	2.14E-03
15NC88*	Massif du Sud	Harzburgite	Xu et al. (2020)	-	-	-	-	955	851	910	-	-	1.0	2.14E-03

T_{REE-Y} = REE-Y-in-two-pyroxene thermometer (Liang et al., 2013); $T_{BKN}-T_{Ta}$ = two-pyroxene solvus thermometers (Brey and Köhler, 1990; Taylor, 1998); $T_{Ca-in-Opx}$ = Ca in orthopyroxene thermometer (Brey and Köhler, 1990); $T_{Ca-in-Ol}$ = Ca in olivine thermometer (De Hoog et al., 2010); T_{Ol-Sp} = olivine-spinel Fe-Mg thermometer (Li et al., 1995). s: standard deviation of calculated T_{REE-Y} . Temperatures were computed using average compositions of porphyroclastic cores and assuming a pressure of 10 kbar.

* Cpx-free harzburgites: for these samples $T_{Ca-in-Opx}$ represent minimum temperature estimates under the assumption that orthopyroxene composition reflects equilibrium with clinopyroxene.

‡ Olivine grain radius = average olivine grain radius used for calculations of cooling rates based on $T_{Ca-in-Ol}$. Olivine grain radius was deduced from petrographic observations for samples from the works of Secchiari et al. (2016, 2020). For literature data (Marchesi et al., 2009; Pirard et al., 2013; Xu et al., 2020) an average olivine grain radius of 1 mm was assumed. See text for further details.

Table 2. Equilibrium temperatures and cooling rates calculated for the New Caledonia mafic and ultramafic intrusives.

Sample	Locality	Lithology	Note	Source	P (kbar)	T _{Pl-Cpx}	1σ	T _{BKN}	T _{Ta}	T _{Ca-in-Opx}	T _{Ca-in-Ol}	T _{Ol-Sp}	Ol radius (mm) ²	dT/dt (°C/y) from T _{Ca-in-Ol}
CDM1*	Col de Mouirange	Wehrlite	Cumulate	Secchiari et al., unpubl.	3	-	-	-	-	889	-	877	-	-
CDM2	Col de Mouirange	Spl dunitite	Cumulate	Secchiari et al., unpubl.	-	-	-	-	-	-	-	844	-	-
CDM3	Col de Mouirange	Gabbro-norite	Cumulate	Secchiari et al. (2018)	2	-	-	-	-	-	730	-	0.5	4.66E-04
CDM6	Col de Mouirange	Gabbro-norite	Cumulate	Secchiari et al. (2018)	2	-	-	-	-	-	707	-	0.5	2.49E-04
PL1*	Plum	Gabbro-norite	Cumulate	Secchiari et al. (2018)	1.9**	1241	43	-	-	926	734	-	0.5	5.19E-04
PR2B	Rivière des Pirogues	Gabbro-norite	Cumulate	Secchiari et al. (2018)	2	-	-	-	-	-	730	-	0.5	4.66E-04
PR3*	Rivière des Pirogues	Gabbro-norite	Cumulate	Secchiari et al. (2018)	2	1243	23	-	-	980	718	-	0.5	3.37E-04
PR4	Rivière des Pirogues	Ol clinopyroxenite	Cumulate	Secchiari et al., unpubl.	-	-	-	-	-	-	-	942	-	-
PRO3b	Prony	Gabbro-norite	Cumulate	Secchiari (2016)	2.8**	-	-	1054	1030	1040	-	866	-	-
PR1B*	Prony	Opx-gabbro-norite		Marchesi et al. (2009)	2	-	-	-	-	1066	819	-	0.5	4.18E-03
PR3A	Prony	Opx-gabbro-norite		Marchesi et al. (2009)	2	-	-	964	957	925	684	-	0.5	1.29E-04
MS36	Montagne des Sources	Pl-dunite		Marchesi et al. (2009)	-	-	-	-	-	-	-	904	-	-
MS20	Montagne des Sources	Pl-Wehrlite		Marchesi et al. (2009)	3.2**	-	-	967	942	1087	853	886	0.8	3.45E-03
MS22	Montagne des Sources	Pl-Wehrlite		Marchesi et al. (2009)	3**	-	-	1008	967	1114	796	839	0.8	9.58E-04
MS28*	Montagne des Sources	Pl-Wehrlite		Marchesi et al. (2009)	3	-	-	-	-	1055	853	-	0.8	3.46E-03
MS30*	Montagne des Sources	Pl-Wehrlite		Marchesi et al. (2009)	3	-	-	-	-	1099	853	-	0.8	3.46E-03
MS31*	Montagne des Sources	Pl-Wehrlite		Marchesi et al. (2009)	3	-	-	-	-	1105	827	-	0.8	1.98E-03
MS32*	Montagne des Sources	Pl-Wehrlite		Marchesi et al. (2009)	3	-	-	-	-	1036	853	844	0.8	3.45E-03
MS35	Montagne des Sources	Opx-gabbro-norite		Marchesi et al. (2009)	2	-	-	1034	1019	1110	-	-	-	-
MS37	Montagne des Sources	Cpx-dunite		Marchesi et al. (2009)	-	-	-	-	-	-	-	880	-	-
MS38	Montagne des Sources	Dunite		Marchesi et al. (2009)	-	-	-	-	-	-	-	884	-	-
MS39	Montagne des Sources	Dunite		Marchesi et al. (2009)	-	-	-	-	-	-	-	856	-	-
MS40	Montagne des Sources	Dunite		Marchesi et al. (2009)	-	-	-	-	-	-	-	964	-	-
MDS34*	Montagne des Sources	Wehrlite	Cumulate	Pirard et al. (2013)	3	-	-	-	-	1147	899	970	0.8	8.91E-03
MDS37	Montagne des Sources	Gabbro	Cumulate	Pirard et al. (2013)	2.4**	-	-	1074	1050	1101	869	-	0.5	1.24E-02
MDS43	Montagne des Sources	Dunite	Cumulate	Pirard et al. (2013)	-	-	-	-	-	-	-	982	-	-
MDS49	Montagne des Sources	Dunite	Cumulate	Pirard et al. (2013)	3	-	-	-	-	-	-	886	-	-
RP33	Rivière des Pirogues	Websterite	Cumulate	Pirard et al. (2013)	3	-	-	1087	1081	990	-	-	-	-
RP51	Rivière des Pirogues	Clinopyroxenite	Cumulate	Pirard et al. (2013)	3	-	-	1028	1092	1117	-	-	-	-

T_{Pl-Cpx} = REE-Y in plagioclase-clinopyroxene pair (Sun and Liang, 2017); T_{BKN} - T_{Ta} = two-pyroxene solvus thermometers (Brey and Köhler, 1990; Taylor, 1998); T_{Ca-in-Opx} = Ca in orthopyroxene thermometer (Brey and Köhler, 1990); T_{Ca-in-Ol} = Ca in olivine thermometer (De Hoog et al., 2010); T_{Ol-Sp} = olivine-spinel Fe-Mg thermometer (Li et al., 1995). T were computed using averaged composition of crystal cores.

* Cpx-free mafic and ultramafic intrusives: for these samples T_{Ca-in-Opx} represent minimum temperature estimates under the assumption that orthopyroxene composition reflects equilibrium with clinopyroxene.

** = Pressure calculated following the method of Fumagalli et al. (2017).

‡ Olivine grain radius = average olivine grain radius used for calculations of cooling rates based on T_{Ca-in-Ol}. Olivine grain radius was deduced from petrographic observations for samples from the work of Secchiari et al. (2018). For the other literature works (Marchesi et al., 2009; Pirard et al., 2013) an average olivine grain radius of 0.5 mm and 0.8 mm was assumed for the gabbro-norites and the wehrlites, respectively.

Table 3. Summary of the temperatures recorded by the main lithologies belonging to the New Caledonia Nappe

Lithology	T _{REE} min	T _{REE} max	T _{BKN} min	T _{BKN} max	T _{BKN} average	T _{Ta} min	T _{Ta} max	T _{Ta} average	T _{Ca-in-Opx} min	T _{Ca-in-Opx} max	T _{Ca-in-Opx} average	T _{Ca-in-Ol} min	T _{Ca-in-Ol} max	T _{Ca-in-Ol} average	T _{Oi-Sp} min	T _{Oi-Sp} max	T _{Oi-Sp} average
Lherzolites	1256	1394	776	993	896	758	1026	1046	1010	1082	1046	824	893	855	794	950	885
Harzburgites*	-	-	-	-	-	-	-	-	903	1185	1020	741	938	842	815	1007	924
Mafic-ultramafic intrusives	-	-	964	1083	1027	942	1092	1017	889	1147	1046	684	899	795	839	982	898
Mafic intrusives**	1241	1243	964	1050	1014	957	1050	1014	925	1110	1021	684	819	732	-	-	-
Ultramafic intrusives***	-	-	-	-	-	-	-	-	889	1147	1064	796	899	850	839	982	898
Dunites	-	-	-	-	-	-	-	-	-	-	-	-	-	-	844	964	888

T_{REE} indicates REE-Y-in-two-pyroxene thermometer (Liang et al.; 2013) for the lherzolites and clinopyroxene-plagioclase thermometer (Sun and Liang, 2017) for the gabbronorites; T_{BKN}-T_{Ta} = two-pyroxene solvus thermometers

(Brey and Köhler, 1990; Taylor, 1998); T_{Ca-in-Opx} = Ca in orthopyroxene thermometer (Brey and Köhler, 1990); T_{Ca-in-Ol} = Ca in olivine thermometer (De Hoog et al., 2010); T_{Oi-Sp} = olivine-spinel Fe-Mg thermometer (Li et al., 1995).

* Cpx-free harzburgites: for these samples T_{Ca-in-Opx} have to be considered as minimum estimates under the assumption that orthopyroxene composition reflects equilibrium with clinopyroxene

** Mafic intrusives = opx-gabbros and gabbronorites.

*** Ultramafic intrusives= wehrlites and pyroxenites